OPECAL

D12:ATBD BAND-TO-BAND INTERCALIBRATION USING THE SUN GLINT OVER OCEAN

TECHNICAL NOTE

	Name	Company	Date	Signature
Prepared by :	B. Berthelot	Magellium	04/12/2014	
Checked by :				
Approved by :	B. Berthelot	Magellium	04/12/2014	

Document reference :	OPECAL-TN-022-MAG
Issue.Revision :	2.1
Date :	04/12/2014
Client :	ESRIN
Ref., Tender :	AO/1-7043/11/F/MOS

This document is the property of Magellium. It cannot be reproduced, nor communicated without written permission.

Distribution list

	Name	Company	N. copies
Addresses :	M. Bouvet G. Ottavianelli	ESA/ESTEC ESA/ESRIN	1
Internal copy :	Customer file Project Manager Development team	Magellium Magellium Magellium	1 (digital) 1 (digital) 1 (digital)

Document Change Record

Iss.	Rev.	Date	Reason	Comments
1	0	27/06/2013	Creation of the document	
2	0	01/11/2014	Results insertion	
2	1	03/12/2014	Answers to ESA comments	

This document is the property of Magellium. It cannot be reproduced, nor communicated without written permission.

Table of contents

1 Objectives of the document 9
1.1 Related documents 9
1.1.1 Applicable documents 9
1.1.2 Reference documents 9
1.1.3 Bibliography 10
1.1.4 Acronyms 10
2 Introduction 12
3 Algorithm overview 13
3.1 Principle of the method 13
3.1.1 Method 13
3.1.2 RTM Model 14
3.1.3 Sunglint modelling 15
3.1.3.1 Cox and Munk model description 15
3.1.3.1.1 Calculation of slope distribution 16
3.1.3.1.2 Calculation of Fresnel reflection 17
3.1.3.1.3 Magnitude of contribution 18
3.2 Implementation description 19
3.2.1 Overall steps 19
3.2.2 Detailed steps 19
3.2.2.1 Input data selection 19
3.2.2.2 Auxiliary data extraction 20
3.2.2.3 Pixel selection 20
3.2.2.3.1 Sunglint spot detection 20
3.2.2.3.2 Clear pixel selection 20
3.2.2.3.3 Valid pixel selection 20
3.2.2.3.4 Foam masking 20
3.2.2.3.5 High NIR reflectance 20
3.2.2.4 Gazeous transmission correction 21
3.2.2.5 RTM Solar Irradiance correction 21
3.2.2.6 Windspeed estimation in the reference band 23
3.2.2.7 $\Delta\rho$ estimation in the blue, NIR, and SWIR band 23
3.2.2.8 Statistical analysis of the sensor radiometry 24
3.2.3 Auxiliary data 24
3.2.3.1 Thresholds 24
3.2.3.2 Generation of LUTS 24
3.2.3.2.1 Constants 25
3.2.3.2.2 Look Up tables 26
3.2.4 Ancillary data 27
4 Dataset analysis to monitor the sensor radiometry using sunglint 28
4.1 Introduction 28
4.2 Site selection 28
4.3 Data selection 29
4.4 Analysis of MODIS 29

This document is the property of Magellium. It cannot be reproduced, nor communicated without written permission.

4.4.1 Over SIO 29
4.4.1.1 Details of results for a single date 29
4.4.1.2 Multiyear results 38
4.5 Analysis of MERIS 40
4.5.1 Over SIO 40
4.5.1.1 Details of results for a single date 40
4.5.1.2 Multiyear results 47
4.6 Analysis of POLDER 48
4.6.1 Over SIO 48
4.6.1.1 Details of results for a single date 48
4.6.1.2 Multiyear results 59
4.7 Analysis of AASTR 59
4.7.1 Over SIO 59
4.8 Analysis of ASTR-2 59
4.8.1 Over SIO 59
5 Sensitivity study 60
5.1 Introduction 60
5.2 Initial conditions 60
5.3 Sensitivity to aerosol optical thickness 61
5.4 Sensitivity to water vapour content 61
5.5 Sensitivity to ozone content 62
5.6 Sensitivity to aerosol model 62
5.7 Conclusion 62
6 Error analysis 65

This document is the property of Magellium. It cannot be reproduced, nor communicated without written permission.

List of the Tables

Table 1: List of applicable documents 9
Table 2: List of reference documents 9
Table 3: Solar irradiance 22
Table 4: Spectral band used for wind speed retrieval 23
Table 5: Spectral band used for radiometry monitoring over sunglint target 24
Table 6: Thresholds used to select data 24
Table 7: Summary of the constants used to generate the LUT 25
Table 8: Solar and view zenith/azimuth angles for SIO and SPG sites. SZA, VZA, SAA an VAA stand for Solar Zenith Angle, View Zenith Angle, Solar Azimuth Angle, View Azimuth Angle respectively. 26
Table 9: Range of variation of 6SV variables 26
Table 10: Range of variation of wind speed variables 27
Table 11: Ancillary data needed in the Sunglint method 27
Table 12: Ocean site location 28
Table 13: Input data 60

This document is the property of Magellium. It cannot be reproduced, nor communicated without written permission.

List of the Figures

Figure 1: Definition of the wave angle θn....16
Figure 2: Spectral variability of refraction index 17
Figure 3: Reflectance of the sunglint at 0.45, 0.67, 0.87 and 1.61 µm for a wind speed varying from 1 to 10 m/s 18
Figure 4: Reflectance of the sunglint versus wavelength for a wind speed varying of 2, 4 and 6 m/s....18
Figure 5: Reflectance of the sunglint at 870 nm in the principal plane for a wind speed of 2, 4 and 6 m/s. 18
Figure 6: Spectral dependence of the aerosol optical thickness for ,the selected model .25
Figure 7: MODIS acquisition 07/01/2010 (Product MYD021KM.A2010007.0820.005.2010008134354.gscs_000500561122_hdf) 30
Figure 8: TOA reflectances in MODIS Reflected Solar bands 1-7, 26....31
Figure 9: Wave angle for the acquisition (left). Zoom inside the selected sunglint (right) area. Geographic representation. 32
Figure 10: TOA reflectances in channels 1 and 2, and wave angle....32
Figure 11: Windspeed (m/s), Water vapour content (g/cm2) and ozone content (cm.atm) in the sunglint spot....33
Figure 12: Cloud mask 34
Figure 13: Control of the windspeed retrieval 34
Figure 14: Estimated wind speed....35
Figure 15: Difference between ERA wind speed and estimated wind speed 35
Figure 16: Scatterplot of simulated TOA reflectances versus measured TOA reflectances36
Figure 17: TOA reflectance in the NIR. Measured (top left), Simulated (top right), difference estimated minus measured (bottom)....36
Figure 18: Measured to Simulated TOA reflectance ratio in the NIR versus estimated wind speed 37
Figure 19: Map of Ak in the NIR band 37
Figure 20: Ratio of Measured to Simulated TOA reflectance histograms....37
Figure 21: Temporal variability of mean ratio between 2002 and 2011 – NIR band 38
Figure 22: Temporal acquisition of mean ratio between 2002 and 2011 – BLUE band....38
Figure 23: Temporal acquisition of mean ratio between 2002 and 2011 – SWIR band ...39
Figure 24: MERIS acquisition 23/11/2008 (Product MER_RR__1PRMAP20081123_044118_000001832074_00076_35200_0001_N1) 40
Figure 25: TOA reflectances in MERIS Reflected Solar bands 13 41
Figure 26: Wave angle inside the sunglint area 41
Figure 27: TOA reflectances in channels 7 and 13, and wave angle....42
Figure 28: Windspeed, Water vapour content and ozone content....42
Figure 29: Cloud mask 43
Figure 30: Control of the windspeed retrieval....43
Figure 31: Estimated windspeed....44
Figure 32: Difference between ERA wind speed and estimated wind speed 44
Figure 33: Scatterplot of simulated TOA reflectances versus measured TOA reflectances45
Figure 34: TOA reflectance in the NIR. Measured (top left), Simulated (top right), difference estimated minus measured bottom 45

This document is the property of Magellium. It cannot be reproduced, nor communicated without written permission.

Figure 35: Measured to Simulated TOA reflectance ratio in the NIR versus estimated wind speed 46
Figure 36: Map of Ak in the NIR band 46
Figure 37: Reflectance ratio histograms 46
Figure 38: Temporal acquisition of mean ratio between 2002 and 2011 – NIR band 47
Figure 39: Temporal acquisition of mean ratio between 2002 and 2011 – BLUE band 47
Figure 40: PARASOL acquisition 02/03/2011 (Product P3L1TBG1143099KD_s25_00_S35_00_e075_00_E110_00) 48
Figure 41: PARASOL image sequence containing the sunglint. Sequences are croissant from left to right. 49
Figure 42: TOA reflectance inside Sunglint area (Left). Wave angle inside the sunglint area for PARASOL direction 1 50
Figure 43: TOA reflectance inside Sunglint area (Left). Wave angle inside the sunglint area for PARASOL direction 2 50
Figure 44: TOA reflectance inside Sunglint area (Left). Wave angle inside the sunglint area for PARASOL direction3 51
Figure 45: TOA reflectance inside Sunglint area (Left). Wave angle inside the sunglint area for PARASOL direction 4 51
Figure 46: TOA reflectance inside Sunglint area (Left). Wave angle inside the sunglint area for PARASOL direction 5 51
Figure 47: TOA reflectance inside Sunglint area (Left). Wave angle inside the sunglint area for PARASOL direction 6 51
Figure 48: TOA reflectance inside Sunglint area (Left). Wave angle inside the sunglint area for PARASOL direction 7 52
Figure 49: TOA reflectance inside Sunglint area (Left). Wave angle inside the sunglint area for PARASOL direction 8 52
Figure 50: TOA reflectance inside Sunglint area (Left). Wave angle inside the sunglint area for PARASOL direction 9 52
Figure 51: TOA reflectance inside Sunglint area (Left). Wave angle inside the sunglint area for PARASOL direction 10 53
Figure 52: TOA reflectance inside Sunglint area (Left). Wave angle inside the sunglint area for PARASOL direction 11 53
Figure 53: TOA reflectance inside Sunglint area (Left). Wave angle inside the sunglint area for PARASOL direction 12 53
Figure 54: TOA reflectance inside Sunglint area (Left). Wave angle inside the sunglint area for PARASOL direction 13 54
Figure 55: TOA reflectance inside Sunglint area (Left). Wave angle inside the sunglint area for PARASOL direction 14 54
Figure 56: TOA reflectance inside Sunglint area (Left). Wave angle inside the sunglint area for PARASOL direction 15 54
Figure 57: Maximum TOA reflectance inside Sunglint area (Left). Minimum wave angle computed from the 16 directions 55
Figure 58: Windspeed, Water vapour content and ozone content 55
Figure 59: Cloud mask 56
Figure 60: Control of the wind speed retrieval 56
Figure 61: Estimated wind speed 57
Figure 62: Scatterplot of simulated TOA reflectances versus measured TOA reflectances 57
Figure 63: Measured to Simulated TOA reflectance ratio in the NIR versus estimated wind speed 58

This document is the property of Magellium. It cannot be reproduced, nor communicated without written permission.

Figure 64: Map of Ak in the NIR band 58
Figure 65: Reflectance ratio histograms (Top, NIR channel; Bottom, BLUE channel) 58
Figure 66: Temporal acquisition of mean ratio between 2006 and 2011 – NIR band.....59
Figure 67: Temporal acquisition of mean ratio between 2006 and 2011 – BLUE band....59
Figure 68: MERIS spectrum for the sensitivity study 61
Figure 69: Aerosol optical thickness temporal variability since 06/2002 (Dataset MYD08_M3) over SIO.....63
Figure 70: Angstrom exponent temporal variability since 06/2002 (Dataset MYD08_M3) over SIO.....63
Figure 71: Spectral AOT variability for 17 models. AOT(550 nm)=0.05. M, ...64

This document is the property of Magellium. It cannot be reproduced, nor communicated without written permission.

1 Objectives of the document

The purpose of this study is to develop and implement a method for calibrating optical sensors using sunglint target into DIMITRI software.

1.1 Related documents

1.1.1 Applicable documents

Table 1: List of applicable documents

Id.	Ref.	Description
AD1	QA4EO-QAEO-GEN-DQK-001/7, Version 4.0	QA4EO Guidelines (seven documents) http://qa4eo.org/

1.1.2 Reference documents

Table 2: List of reference documents

Id.	Ref.
RD 1.	Bouvet M., Ramonio F., Radiometric intercomparison of AATSR, MERIS, and Aqua MODIS over Dome Concordia (Antarctica), Can. J. Remote Sensing, Vol. 36, No. 5, pp. 464–473, 2010. http://pubs.casi.ca/loi/cjrs
RD 2.	DIMITRI Software User Manual ftp://ftp.estec.esa.int/pub/gsp/anonymous/Earth_Observation_Multi-mission_Phase-E2_Operational_Calibration/DIMITRI_SUM.pdf
RD 3.	DIMITRI Software Design Document ftp://ftp.estec.esa.int/pub/gsp/anonymous/Earth_Observation_Multi-mission_Phase-E2_Operational_Calibration/DIMITRI_SDD.pdf
RD 4.	Statement of Word GSP activity 'Towards the Intercalibration of EO Medium Resolution Multi-Spectral Imagers' ftp://ftp.estec.esa.int/pub/gsp/anonymous/Earth_Observation_Multi-mission_Phase-E2_Operational_Calibration/SoW_GSP_TowardsTheIntercomparisonOfEOMediumResolutionMultiSpectralImagers.pdf
RD 5.	Hagolle et Al., Results of POLDER in-flight Calibration, IEEE Transactions on Geoscience and Remote Sensing, May 1999, Volume 37, Number 03 [p. 1550]. http://ieeexplore.ieee.org/xpl/RecentIssue.jsp?punumber=36
RD 6.	Vermote, E., R. Santer, P.Y. Deschamps and M. Herman, In-flight Calibration of Large Field-of-View Sensors at Short Wavelengths using Rayleigh Scattering, Int. Journal of Remote Sensing, 13, No 18, 1992. http://www.tandf.co.uk/journals/tres

This document is the property of Magellium. It cannot be reproduced, nor communicated without written permission.

RD 7.	Smith D., Poulsen C., Latter B.: Calibration Status of the AATSR Reflectance Channels, MERIS AATSR workshop 2008 proceedings. http://earth.esa.int/meris_aatsr_2008/

1.1.3 Bibliography

- Ackerman, S. A., K. I. Strabala, W. P. Menzel, R. A. Frey, C. C.Moeller, and L. E. Gumley, 1998: Discriminating clear-sky from clouds with MODIS. J. Geophys. Res., 103 (D24), 32 141–32 157.
- S.Y. Kotchenova, E.F. Vermote, R. Matarrese, and F.J. Klemm, Jr., Validation of a vector version of the 6S radiative transfer code for atmospheric correction of satellite data. Part I: Path Radiance, Applied Optics, 45(26), 6726-6774, 2006.
- S.Y. Kotchenova and E.F. Vermote, Validation of a vector version of the 6S radiative transfer code for atmospheric correction of satellite data. Part II: Homogeneous Lambertian and anisotropic surfaces, Applied Optics, 2007.
- Morel, Optical modeling of the upper ocean in relation to its biogenous matter content (case I waters), Journal of Geophysical Research, 93(C9), 10749-10768, 1988.
- Hagolle, O.; Nicolas, J.-M.; Fougnie, B.; Cabot, F.; Henry, P., "Absolute calibration of VEGETATION derived from an interband method based on the Sun glint over ocean," Geoscience and Remote Sensing, IEEE Transactions on , vol.42, no.7, pp.1472,1481, July 2004.
- M. Born, and E. Wolf, Principles of Optics - fifth edition, Pergamon Press, New-York, 1975.
- Cox, and W. Munk, Statistics of the sea surface derived from sun glitter, Journal of Marine Research, 13, 198-227, 1954.
- Cox, and W. Munk, Measurement of the roughness of the sea surface from photographs of the sun's glitter, Journal of the Optical Society of America, 44, 838-850, 1954.
- Cox, and W. Munk, Some problems in optical oceanography, Journal of Marine Research, 14, 63-78, 1955.
- Nicolas J.-M., P.-Y. Deschamps and O. Hagolle, 2006: Radiometric Calibration of the Visible and Near-Infrared Bands of Seviri Using Rayleigh Scattering and Sun-Glint Over Oceans. Proceedings of the 3rd MSG RAO Workshop (ESA SP-619). 15 June 2006, Helsinki, Finland. Editor: D. Danessy, p.19.
- H. Neckel, and D. Labs, The solar radiation between 3300 and 12500, Solar Physics, 90, 205-258, 1984.
- Vermote E. and D. Tanré, 1992, Analytical expressions for radiative properties of planar Rayleigh scattering media including polarization contribution. Journal of Quantitative Spectroscopy and Radiative Transfer, 47, 305-3 14.
- Jolivet et al., 2009, In-flight Calibration of Seviri Solar Channels on board MSG Platforms, Eumetsat User Meeting.

1.1.4 Acronyms

6SV	Second Simulation of a Satellite Signal in the Solar Spectrum, Vector
AATSR	Advanced Along Track Scanning Radiometer
ADEOS	Advanced Earth Observation Satellite
ATSR	Along Track Scanning Radiometer
ATCOR	ATmospheric CORrection

This document is the property of Magellium. It cannot be reproduced, nor communicated without written permission.

AVHRR	Advanced Very High Resolution Radiometer
BOUSSOLE	BOUée pour l'acquiSition d'une Série Optique à Long termE
BRDF	Bidirectional Reflectance Distribution Function
Cal/Val	CALibration and VALidation
CEOS	Committee on Earth Observation Satellites
CNES	Centre National d'Etudes Spatiales
CVI	Cal/Val interest
DIMITRI	Database for Imaging Multispectral Instruments and Tools for Radiometric Intercomparison
DN	Digital Number
ENVISAT	ENVIronment SATellite
EO	Earth Observation
ESA	European Space Agency
IVOS	Infrared and Visible Optical Sensors
LandNet	Land Network
MERIS	Medium Resolution Imaging Spectrometer
MODIS	Moderate Resolution Imaging Spectroradiometer
MODTRAN	Moderate-Resolution Atmospheric Radiance and Transmittance Model
NASA	National Aeronautics and Space Administration
NOAA	National Oceanic and Atmospheric Administration
PARASOL	Polarization & Anisotropy of Reflectances for Atmospheric Sciences coupled with Observations from a Lidar
POLDER	POLarization and Directionality of the Earth's Reflectances
QA4EO	Quality Assurance Framework for Earth Observation
RADTRAN	Radiative Transfer
RIM	Radiometric Instrument Model
ROSAS	RObotic Station for Atmosphere and Surface
RTM	Radiative Transfer Model
SADE	Structure d'Accueil de Données d'Etalonnage
SNR	Signal to Noise Ratio
SWIR	Short Wave Infra-Red
TOA	Top Of Atmosphere
VGT	VEGETATION
VIS	VISible
WG	Working Group
WGCG	Working Group on Calibration and Validation

This document is the property of Magellium. It cannot be reproduced, nor communicated without written permission.

2 Introduction

This Algorithm Theoretical Basis Document describes the algorithm used to estimate the Band-to-band intercalibration using the Sun glint over ocean. In particular, this document identifies sources of input data, both satellite and auxiliary data. It provides the physical theory and mathematical background underlying the use of this information in the method. It includes implementation details, and describes assumptions and limitations of the adopted approach.

This task is referred by task 3 of the SOW.

The software processes images acquired over the sites by AATSR, MODIS/Aqua, MERIS, and PARASOL instruments.

This document is the property of Magellium. It cannot be reproduced, nor communicated without written permission.

3 Algorithm overview

3.1 Principle of the method

The Sun glint calibration method is an interband calibration method that uses the specular reflection of the Sun on the ocean surface to transfer the absolute calibration of one reference spectral band to other spectral bands. It provides accurate calibration results for near-infrared spectral (NIR) bands up to Short wave Infrared band (SWIR) (Hagolle et al., 1999).

The sunglint is characterized by a spectrally flat and high radiance. This high signal level limits the influence of other parameters such as water leaving radiance or aerosols. The sunglint reflectance depends mainly on the sea-surface roughness, which is related to the wind speed. The ratio of the spectral reflectances for regions in sun glint is insensitive to surface wind speed.

The principle of the sun glint calibration method is to compare the measurements provided by the sensor above sun glint to a simulation of the top-of-atmosphere reflectance (Eq. 1). This ratio is computed for all acquisitions and monitored on a large period of time to detect possible change in sensor radiometry.

$$\Delta\rho = \frac{\rho_{TOA}^{Measured}}{\rho_{TOA}^{Simulated}} \quad \textbf{Eq. 1}$$

In this ATBD, we will describe the method implemented to monitor the temporal variability of this ratio.

3.1.1 Method

The principle is to simulate TOA reflectances in sunglint spot and compared it to the satellite measurement.

The Top Of the Atmosphere reflectance corrected from the gaseous transmission is modelled as the sum of the reflectance of all contributors to the signal:

$$\rho_{TOA}^{Measured} = \rho_m + \rho_a + \rho_{ma} + (1-f)T_m T_a \rho_{sun} + t_m t_a\left((1-f)\rho_w + f\cdot\rho_f\right) \quad \textbf{Eq. 2}$$

where ρ_m is the reflectance due to molecular scattering (or Rayleigh scattering), ρ_a is the aerosol reflectance, ρ_{ma} is a multiple scattering term modelling the interaction between aerosols and molecules, ρ_w is the marine reflectance at sea level (i.e. the marine radiance normalised by the solar irradiance at sea level), ρ_f is the foam reflectance at sea level, f is the pixel fraction covered by foam (the more wind the higher f), $t_m t_a$ is the product of the diffuse transmittances of molecules and aerosols, respectively, along the path Sun to surface and surface to satellite. The reflectance denoted ρ_{sun} is due to the specular reflection of the Sun on sea surface and it is weighted by the direct transmission of the atmosphere from surface to satellite, $T_m T_a$. The coupling between Fresnel reflection and atmospheric scattering is taken into account in the atmospheric terms ρ_m and ρ_a. This linearization is based on a large-scale

This document is the property of Magellium. It cannot be reproduced, nor communicated without written permission.

formalism, in which adjacency effects are neglected. It is not applicable to pixels contaminated by the presence of land.

Equation above is only valid when gaseous absorption and scattering effects may be decoupled. This is the case for most spectral bands in the visible domain except for the bands in which strong oxygen and water vapour absorption occurs.

For areas where foam is negligible, the equation is simplified, and the TOA reflectance over sunglint can be written:

$$\rho_{TOA}^{Measured} = \rho_m + \rho_a + \rho_{ma} + T_m T_a \rho_{sun} + t_m t_a \rho_w \quad \textit{Eq. 3}$$

A radiative transfer model is used to simulate the top of atmosphere reflectances, accounting for the geometrical configurations of the observations, and surface and atmosphere conditions at the time of acquisitions.

3.1.2 RTM Model

We choose to use 6SV1 RTM to perform the simulations and estimate all terms of equation 2.

6SV1 RTM is a reference model used to perform accurate simulations of the solar radiation reflected by the surface-atmosphere system as measured by satellite and plane observation, accounting for elevated targets, use of anisotropic and lambertian surfaces and calculation of gaseous absorption. The code is based on the method of successive orders of scatterings approximations and is able to account for radiation polarization (Kotchenova et al., 2006; Kotchenova and Vermote, 2007).

Simulations are performed for all spectral bands of the reference sensor, the geometrical illumination and observation conditions, an atmosphere described by an aerosol model and an optical thickness, an atmospheric profile depending on the latitude, water vapour and ozone content, a sunglint reflectance and a water leaving reflectance.

1) 6S allows the coupling between ocean and atmosphere.
2) A water leaving reflectance model is available in 6S (Morel, 1988). It depends on chlorophyll concentration level.
3) Sunglint reflectance model is available in 6S based on Cox and Munk model, 1954.

At least there are two possibilities to simulate the TOA reflectances.

1) Method 1 : Direct modelling using RTM

   The method runs the RTM in a direct way for the set of selected inputs. The comparison is performed directly.

   This solution is probably the best because it does not introduce methodological errors but is not applicable due to the computation time.
2) Method 2: Use pre computed Look Up Tables of output of RTM

   The method is based on the use of Look Up Tables containing simulated TOA reflectances for a large range of variations of the inputs parameters and the search the actual configuration which is closest to the simulation.

This document is the property of Magellium. It cannot be reproduced, nor communicated without written permission.

3.1.3 Sunglint modelling

3.1.3.1 Cox and Munk model description

The phenomenon of ocean sun glint, the specular reflection of direct sun light at the ocean surface, was explored by Cox and Munk (1954a). They established an empirical relation between the surface wind field and the slope distribution of the wave facets from comparisons of aerial photographs with wind speed measurements at the surface.

They derived an analytical model for the sea surface reflectance based on Fresnel's equations and the distribution for the orientation of reflecting surface irregularities called facets. It was found that the distribution of wave slopes can be reasonably well approximated by a Gaussian function.

The sun glint depends on the following parameters:

- Solar zenith angle θ_s and azimuth angle ϕ_s;
- Viewing zenith angle θ_v and azimuth angle ϕ_v
- Wavelength,λ.
- Real component n of refractive index.
- Wind speed ws , measured in $m.s^{-1}$
- Wind direction. Rotating clockwise from north by the wind azimuth ϕ_{ws}. $\chi=\phi_s-\phi_{ws}$.

The sun glint reflectance is expressed as:

$$\rho_{sungl\,\mathrm{int}} = \frac{\pi R(n,\theta_s,\theta_s,\theta_s,\theta_s)}{4\cos(\theta_s)\cos(\theta_v)\cos(\theta_n{}^4)} P_{sungl\,\mathrm{int}} \quad \textit{Eq. 6}$$

Where

- $R(n,\theta s,\theta v,\phi s,\phi v)$ is the Fresnel, reflection coefficient;
- n is the complex index of refraction of sea water;
- $P_{sunglint}$ is the wave slope probability distribution function;
- θn is the wave angle;

θn is defined as a function of θs, θv and θp, where θp is the phase angle, i.e. the angle between sun direction and satellite direction. θn and θp are defined by the following equations:

$$\cos(\theta_n) = \frac{\cos(\theta_s)+\cos(\theta_v)}{2\cos(\frac{\theta_p}{2})} \quad \textit{Eq. 7}$$

$$\cos(\theta_p) = \cos(\theta_s)\cos(\theta_v)+\sin(\theta_s)\sin(\theta_v)\cos(d\phi) \quad \textit{Eq. 8}$$

This document is the property of Magellium. It cannot be reproduced, nor communicated without written permission.

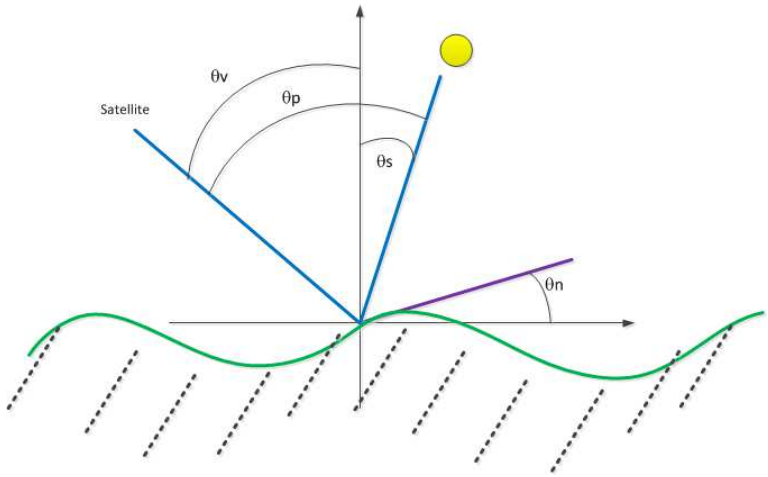

Figure 1: Definition of the wave angle θn

The detail of the model is provided in the paragraph below.

3.1.3.1.1 Calculation of slope distribution

The algorithm defines a coordinate system (P,X,Y,Z) such that P is the observed point on the surface and Z the altitude with PY in the direction of the Sun and PX in the direction perpendicular to the Sun's plane. The surface slope is defined by the following two components:

$$Z_x = \frac{\delta Z}{\delta X} = \sin(\alpha)\tan(\theta_n) \quad \textit{Eq. 7}$$

$$Z_y = \frac{\delta Z}{\delta Y} = \cos(\alpha)\tan(\theta_n) \quad \textit{Eq. 8}$$

where α is the azimuth of the ascent (clockwise from the sun) and θn is the tilt. Using spherical trigonometry, Z_x and Z_y can be related to the incident and reflected directions ($\pi / 2 \geq \theta s$ and $\theta v \geq 0$) as :

$$Z_x = \frac{-\sin(\theta_v)\sin(\phi s - \phi v)}{\cos(\theta_s) + \cos(\theta_v)} \quad \textit{Eq. 9}$$

$$Z_y = \frac{\sin(\theta_v) + \sin(\theta_v)\cos(\phi s - \phi v)}{\cos(\theta_s) + \cos(\theta_v)} \quad \textit{Eq. 10}$$

For the case of an anisotropic distribution of slope components (dependent on the wind direction), the axes can be rotated clockwise from the north by χ to define a new coordinate system (P,X',Y',Z) where PY is parallel to the wind direction. The slope components are now expressed as:

$$Z_x' = \cos(\chi)Z_x + \sin(\chi)Z_y \quad \textit{Eq. 11}$$

$$Z_y' = \sin(\chi)Z_x + \cos(\chi)Z_y \quad \textit{Eq. 12}$$

The slope distribution is described by a Gram-Charlier series:

This document is the property of Magellium. It cannot be reproduced, nor communicated without written permission.

$$P(Z_x^{'},Z_y^{'})=\frac{1}{2\pi\sigma_x^{'}\sigma_y^{'}}e^{\left(-\frac{\xi^2+\eta^2}{2}\right)}\left[\begin{array}{l}1-\frac{1}{2}C_{21}\left(\xi^2-1\right)-\frac{1}{6}C_{03}\left(\eta^3-\eta\right)+\frac{1}{24}C_{40}\left(\xi^4-6\xi^2+3\right)\\+\frac{1}{4}C_{22}\left(\xi^2-1\right)\left(\eta^2-1\right)+\frac{1}{24}C_{04}\left(\eta^4-6\eta^2+3\right)\end{array}\right] \quad \textit{Eq. 13}$$

Terms in this series are given in Cox and Munk and, for a clean surface, are defined as:

$$\xi=\frac{Z_x^{'}}{\sigma_x^{'}},\quad \eta=\frac{Z_y^{'}}{\sigma_y^{'}} \quad \textit{Eq. 14}$$

σ_x' and (σ_y') are the rms values of Z_x' and Z_y', the skewness coefficients C_{21} and C_{03}, and the peakedness coefficients C_{40}, C_{22} and C_{04} are defined by Cox and Munk (1954, 1955) for a clean (uncontaminated) surface.

$(\sigma_x')^2$=0.003 + 0.00192 ws ± 0.002,
$(\sigma_y')^2$ = 0.00316 ws ± 0.004,
C_{21} = 0.01 − 0.0086 ws ± 0.03,
C_{03} = 0.04 − 0.033 ws ± 0.12,
C_{40} = 0. 40 ± 0.23,
C_{22} = 0.12 ± 0.06,
C_{04} = 0.23 ± 0. 41.

3.1.3.1.2 Calculation of Fresnel reflection

The Fresnel reflection coefficient (R(n, θs,θv,ϕs,ϕv) describes the proportion of light hitting the surface that is reflected back. It can be calculated taking into account the refraction indices of sea water and air and the angles of incidence and refraction.

In 6SV, Vermote provides a method to calculate it, referring to Born and Wolf (1975). The refractive index of water varies with wavelength. The complex index of refraction of sea water is deduced from the complex index of refraction of pure water, specified by Hale and Querry (1973).An additional correction of +0.006 is added to the real component due to the salinity and chlorinity of typical seawater.

The spectral variability of the refraction index is plotted in the figure below for three levels of salinity.

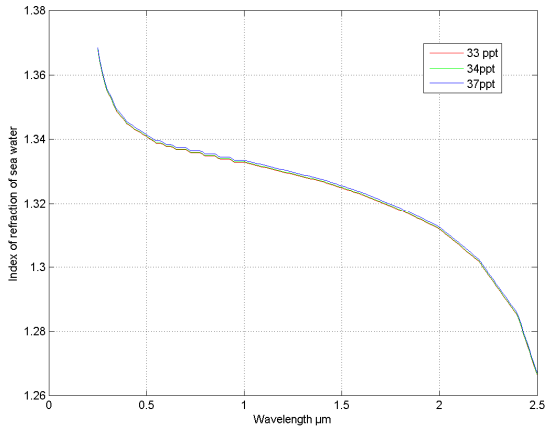

Figure 2: Spectral variability of refraction index

This document is the property of Magellium. It cannot be reproduced, nor communicated without written permission.

3.1.3.1.3 Magnitude of contribution

The three following plots illustrate the variability of the sunglint reflectance for different wavelengths, wind speeds and view angles.

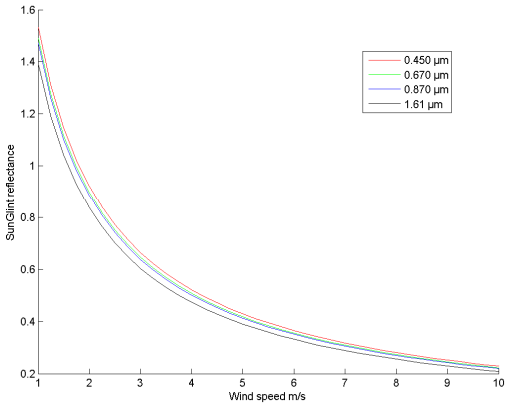

Figure 3: Reflectance of the sunglint at 0.45, 0.67, 0.87 and 1.61 µm for a wind speed varying from 1 to 10 m/s

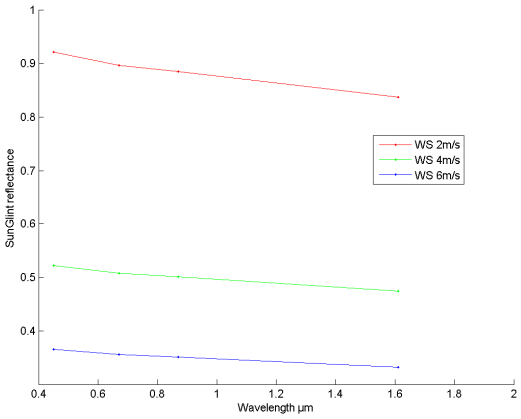

Figure 4: Reflectance of the sunglint versus wavelength for a wind speed varying of 2, 4 and 6 m/s.

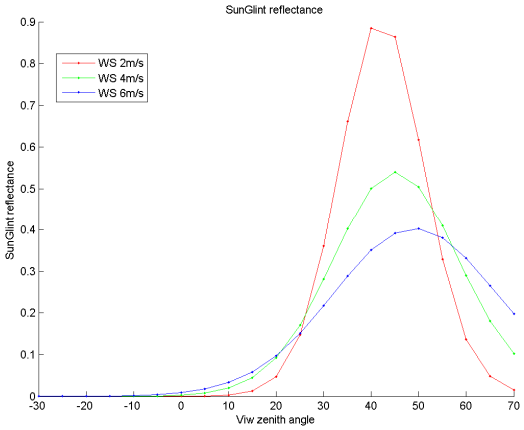

Figure 5: Reflectance of the sunglint at 870 nm in the principal plane for a wind speed of 2, 4 and 6 m/s.

This document is the property of Magellium. It cannot be reproduced, nor communicated without written permission.

3.2 Implementation description

3.2.1 Overall steps

This paragraph provides with the overall steps that have to be done to estimate the ratio of measured out to simulated reflectance.

1) Read the database and select images acquired in the sunglint spot.

   For each selected date (loop)

2) Read the TOA reflectances of clear pixels acquired into the site footprint for the selected date.
3) Read auxiliary data
   - 3.1) Wind speed
   - 3.2) Water vapour content
   - 3.3) Ozone content
4) Check Pixels selection test
   - 4.1) Select valid pixels
   - 4.2) Select clear pixels
   - 4.3) Select NIR TOA pixels such as $\rho NIR > 0.15$
5) Correct TOA reflectances from gaseous absorption
6) Estimate wind speed in the reference band
7) Estimate the TOA reflectance in the bands using estimated windspeed
8) Estimate the reflectance ratio in the blue, NIR, and SWIR band

3.2.2 Detailed steps

3.2.2.1 Input data selection

DIMITRI data ingestion module allows to extract for each acquisition the area which contains the sunglint spot if the geometrical conditions such as defined in paragraph 3.2.2.3.1 are met. One file is written for one acquisition. According to the period selected by the user, these files are read and used as input of the method.

The output file of the ingestion module contains the following information:

- Latitude;
- Longitude;
- Zenith and azimuth solar angles;
- Zenith and azimuth view angles;
- TOA reflectance in all channels;
- Cloud mask ;

This document is the property of Magellium. It cannot be reproduced, nor communicated without written permission.

3.2.2.2 Auxiliary data extraction

Water vapour content, ozone content and wind speed are extracted from ERA dataset for the location of data which contains the sunglint spot. The data are provided each 6 hours. A linear interpolation is performed to estimate the different content at the hour of acquisition.

3.2.2.3 Pixel selection

The selection of pixels is the first step of the processing. The data selected to maximize the sunglint contribution to the measured signal corresponds to the following criteria:

- High sunglint reflectance;
- No clouds;
- No foam;

If the following criteria are not validated, the method is not applied.

3.2.2.3.1 Sunglint spot detection

An automatically selection of acquisitions containing sunglint spot is performed based on the estimation of the wave angle threshold θ_n. This angle is defined as the wave slope that enables having an exact specular reflection given the sun and viewing directions.

All pixels for which $\theta_n < 4°$ are selected.

The threshold has been proposed by Hagolle et al., 2004.

3.2.2.3.2 Clear pixel selection

The clear pixels found in the sunglint area are selected to apply the methodology. The cloud mask is computed in the ingestion procedure, and stored in the acquisition extract containing the sunglint spot. The clear pixel detection is described in the cloud detection ATBD.

Clear pixels are selected.

3.2.2.3.3 Valid pixel selection

It must be noted that Level 1 quality indicators have been used to discard pixels from the processing. Saturated and invalid pixels are removed.

Valid pixels are selected.

3.2.2.3.4 Foam masking

To avoid foam contamination, pixels is selected if the wind speed is lower than the defined threshold (around 5 m/s). The threshold has been proposed by Hagolle et al., 2004.

Pixels for which wind speed is lower than 5 m/s are selected.

3.2.2.3.5 High NIR reflectance

A threshold of 0.15 on the observed sun glint reflectance at 850 nm is applied, to select enough high reflectances to minimize perturbations linked to ocean surface or atmospheric effects (Hagolle et al., 2004).

Pixels for which TOA reflectance in the NIR is lower than 0.15 are selected.

This document is the property of Magellium. It cannot be reproduced, nor communicated without written permission.

3.2.2.4 Gazeous transmission correction

The comparison of the measured reflectance to the estimated one is performed on data corrected from the gaseous transmission. Therefore, it is necessary to estimate the gaseous transmission for each pixel selected by the previous selection step.

The gaseous transmission has been estimated using SMAC formulation.

Analytical formulation is used to simulate the gaseous transmission from the air mass, gaz content (water vapour content, ozone content) and surface pressure. The formulation has been developed first by Rahman and Dedieu, (1996), then improved by Berthelot and Dedieu (2000). SMAC coefficient database has been developed for all optical sensors on orbit up to 2008 by B. Berthelot and is made available for free on CESBIO web site. The coefficients are estimated for H_20, O_3, O_2, CO_2, CH_4, NO_2, CO gaz.

- Input for total gaseous transmission estimation is :
  - Solar zenith angle
  - View zenith angle
  - Water vapour content
  - Ozone content
  - Pressure
  - SMAC coefficients for all bands
- Output is :
  - Total Gazeous transmission.

3.2.2.5 RTM Solar Irradiance correction

The comparison of the TOA reflectance to the simulated one is not direct unless the transformation of radiances to reflectances is performed using the same solar irradiance reference. Indeed, the sensors record raw digital numbers (DN) that are related to the radiances with a sensor radiometric model that can be more or less complex. Once all parameters of this radiometric model estimated, the radiance can be estimated from the measured digital numbers. Then, the TOA reflectances are computed from radiances using the conversion:

$$\rho_{TOA}^{k} = \frac{\pi L^{k}}{E_{os}^{k} (\frac{d_o}{d})^2 \cos(\theta_s)} \quad \textit{Eq. 15}$$

Where k refers to the spectral band, E_{os} is the solar extraterrestrial irradiance in the spectral band k, (d_o/d) is the ratio of Sun-Earth distance at the acquisition date to the mean Sun-Earth distance, and θ_s is the solar zenith angle.

The use of a RTM allows to simulate the apparent reflectance at the satellite level. This reflectance is modelled by:

$$\rho_{6S-TOA}^{k} = \frac{\pi L^{k}}{E_{os-6S}^{k} (\frac{d_o}{d})^2 \cos(\theta_s)} \quad \textit{Eq. 16}$$

Where for this case $E_{os\text{-}6S}$ is the 6S solar extraterrestrial irradiance in the spectral band k. 6S solar irradiance reference is Neckel and Labs, 1984.

This document is the property of Magellium. It cannot be reproduced, nor communicated without written permission.

In order to compare both TOA reflectances, the measured reflectance has to be weighted by the ratio of the solar extraterrestrial irradiance

$$\rho^{k}_{6S-TOA} = \rho^{k}_{TOA} \times \frac{E^{k}_{os}}{E^{k}_{os-6S}} \quad \textbf{Eq. 17}$$

The 6S solar irradiances are reported hereafter for each spectral band in a table where the solar irradiance used for the transformation of radiances to radiances are also provided. The corrective factor is indicated in the last column.

Table 3: Solar irradiance

Sensor	Band number	Central wavelength [nm]	E_{os} sensor (W/m^2)	E_{os-6S} (W/m^2)	E_{os} / E_{os-6S}
MODIS	1	645	1578.11	1603.89	0.984
MODIS	2	858.5	971.74	992.78	0.979
MODIS	3	469	2058.78	2012.55	1.023
MODIS	4	555	1838.69	1859.45	0.989
MODIS	5	1240	454.67	453.66	1.002
MODIS	6	1640	239.77	237.82	1.008
MODIS	7	2130	98.85	95.25	1.038
PARASOL	1	443	1891.16	1897.41	0.997
PARASOL	2	490	1928.39	1935.50	0.996
PARASOL	3	565	1843.69	1842.30	1.001
PARASOL	4	670	1527.45	1532.73	0.997
PARASOL	5	763	1225.40	1229.75	0.996
PARASOL	6	765	1228.45	1232.41	0.997
PARASOL	7	865	980.89	980.40	1.000
PARASOL	8	910	885.09	929.03	0.953
PARASOL	9	1020	712.50	726.33	0.981
MERIS	1	412.5	1716.09	1735.08	0.989
MERIS	2	442.5	1880.34	1858.00	1.012
MERIS	3	490	1929.82	1924.68	1.003
MERIS	4	510	1930.42	1916.12	1.007
MERIS	5	560	1804.47	1845.70	0.978
MERIS	6	620	1652.05	1700.73	0.971
MERIS	7	665	1532.81	1547.51	0.991
MERIS	8	681.25	1473.30	1495.47	0.985
MERIS	9	708.75	1409.03	1394.20	1.011
MERIS	10	753.75	1267.02	1262.78	1.003
MERIS	11	760.625	1255.55	1242.03	1.011
MERIS	12	778.75	1178.17	1192.53	0.988
MERIS	13	865	959.12	972.21	0.987
MERIS	14	885	930.56	975.05	0.954
MERIS	15	900	896.15	943.92	0.949

This document is the property of Magellium. It cannot be reproduced, nor communicated without written permission.

AATSR	1	560	1819.54	1853.11	0.982
AATSR	2	660	1521.89	1546.01	0.984
AATSR	3	862	950.68	971.14	0.979
AATSR	4	1593	254.48	253.03	1.006
VGT	1	460	1963.40	1972.01	0.996
VGT	2	670	1570.30	1551.73	1.012
VGT	3	825	1045.60	1058.47	0.988
VGT	4	1640	234.70	228.24	1.028
ATSR2	1	554			
ATSR2	2	658			
ATSR2	3	864			
ATSR2	4	1608			

3.2.2.6 Windspeed estimation in the reference band

Several authors (Hagolle et al., 2004; Nicolas et al., 2000) mentioned in their papers that the wind speed provided by global models might be not accurate enough to estimate the sun glint reflectance with a good accuracy. The wind speed accuracy is estimated to 2 m/s, which could be not accurate enough for absolute calibration, but interband calibration. Therefore, a procedure is applied to estimate the wind speed in the reference band.

This estimation is an important step of the method. The algorithm estimates the wind speed using the LUT of the reference spectral band such as the simulated TOA reflectance is equalled to the observed one. Then, the wind speed is used to estimate the TOA reflectance that should be measured in the other bands.

The reference bands used for wind speed retrieval are the band centered on 0.670 µm.

Table 4: Spectral band used for wind speed retrieval

Sensor	Spectral band used for wind speed retrieval
MODIS	Band 1
MERIS	Band 7
AATSR	Band 2
ATSR2	Band 2
PARASOL	Band 4

3.2.2.7 $\Delta\rho$ estimation in the blue, NIR, and SWIR band

Once the wind speed estimated, the TOA reflectances in the blue, NIR and SWIR channels are estimated using the LUTs. The search is performed to find the data stored in the LUT which surround the values of the measurements of solar zenith angle, view zenith angle, relative azimuth angle and wind speed in this order. Then the value of the simulated TOA reflectance (normalised to the gaseous transmission) is interpolated between the two last surrounding values at the estimated wind speed.

This document is the property of Magellium. It cannot be reproduced, nor communicated without written permission.

The ratio of TOA reflectances measured out to TOA reflectances estimated is computed for the NIR, SWIR and BLUE bands.

$$\Delta\rho^{Blue} = \frac{\rho_{toa}^{measured}}{\rho_{toa}^{estimated}}, \quad \Delta\rho^{NIR} = \frac{\rho_{toa}^{measured}}{\rho_{toa}^{estimated}}, \quad \Delta\rho^{SWIR} = \frac{\rho_{toa}^{measured}}{\rho_{toa}^{estimated}} \quad \textit{Eq. 18}$$

The table hereafter contains the reference of spectral bands for which the ratio is computed.

Table 5: Spectral band used for radiometry monitoring over sunglint target

Sensor	NIR band	SWIR band	BLUE band
MODIS	Band 2	Band 6	Band 2
MERIS	Band 13		Band 2
AATSR	Band 3	Band 4	Band 1
ATSR2	Band 3	Band 4	Band 1
PARASOL	Band 7		Band 2

As the algorithm is applied on a pixel per pixel basis, a statistical analysis on the ratio is made to remove outliers. Mean and standard deviation of the ratio are estimated and values out of three σ are removed.

3.2.2.8 Statistical analysis of the sensor radiometry

The last step consists in averaging the values of the ratio obtained for one acquisition and monitor it with time.

$$\overline{\Delta\rho} = mean\left(\frac{\rho_{TOA}^{Measured}}{\rho_{TOA}^{Simulated}}\right) \quad \textit{Eq. 19}$$

3.2.3 Auxiliary data

3.2.3.1 Thresholds

The following thresholds have to be defined:

Table 6: Thresholds used to select data

Name	Threshold value
Wind speed (m/s)	5
Wave angle (degrees)	4
Minimum of NIR TOA reflectance	0.15

3.2.3.2 Generation of LUTS

To apply the method, Look Up Tables are computed using the new vectorial version of 6S (6SV, Kotchenova et al., 2007). The first one is dedicated to the wind speed estimation.

This document is the property of Magellium. It cannot be reproduced, nor communicated without written permission.

Spectral bands are indicated in Table 4. The other ones are used to estimate the TOA reflectance in the same conditions as the acquisitions (Table 5).

3.2.3.2.1 Constants

The selected **atmospheric profile** for the simulations is US standard atmosphere.

The **atmospheric pressure** is set to 1013.25 hPa.

Ozone content is 0.3 cm.atm.

The choice of the **aerosol model** is, as recommended by Hagolle et al., 2004, the M98 model, corresponding to a maritime model with 98% humidity. The spectral dependency is represented hereafter:

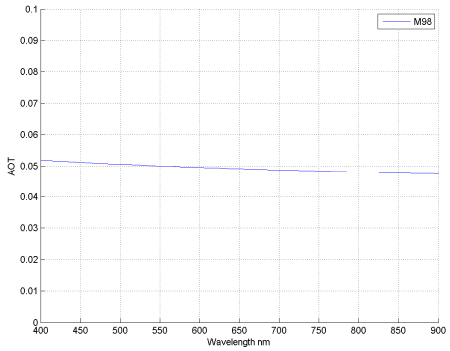

Figure 6: Spectral dependence of the aerosol optical thickness for ,the selected model

A **mean AOT** is used (0.08 at 850 nm) to generate the LUT.

DIMITRI sites, located in the South Pacific Gyre and South Indian Ocean, are inside oligotrophic geographic areas having a priori well-known weak and stable **chlorophyll content** (oligotrophic waters). The chlorophyll concentration is set to 0.05 mg/m^3. This averaged value will be checked in the error budget, by checking with Level 3 data.

Cox and Munk constant variable

In the model, the **sea surface salinity** is set to 34 PSU.

The refraction index is estimated for the spectral bands based on this salinity. It estimates the index of refraction of sea water (nr) and the extinction coefficient of sea water (ni)

Table 7: Summary of the constants used to generate the LUT

Name	Constant value
Atmospheric profile	US62
Aerosol type	M98
Ozone content	0.3 cm.atm
Water vapour content	1.44 g/cm^2
Aerosol optical thickness	0.08 at 550 nm
Chlorophyll concentration	0.05 mg/m^3
Atmospheric pressure	1013.25 hPa

This document is the property of Magellium. It cannot be reproduced, nor communicated without written permission.

SSS	34 PSU
Wind azimuth	0

3.2.3.2.2 Look Up tables

The TOA reflectance corrected from gaseous transmission is computed for a set of varying input for each spectral used in the processing. This LUT is a function of sun zenith angle, view zenith angle, relative azimuth angle, and wind speed.

The sampling is adapted to each sensor, based on the configuration observed on acquisitions.
The minimum and maximum mean angles for SIO site for all the acquisitions available on the database is provided in the table below:

Table 8: Solar and view zenith/azimuth angles for SIO and SPG sites. SZA, VZA, SAA an VAA stand for Solar Zenith Angle, View Zenith Angle, Solar Azimuth Angle, View Azimuth Angle respectively.

Sensor	Site	SZA min	SZA max	VZA min	VZA max	SAA min	SAA max	VAA min	VAA max
PARASOL	SIO	19.6	56.2	6.3	68.0	271.9	326.6	1.4	358.3
	SPG	20.6	66.5	4.3	75.4	269.0	325.7	2.4	358.0
MERIS	SIO	24.2	66.9	2.1	39.1	30.6	89.3	35.0	292.5
	SPG	25.6	67.9	1.0	39.3	29.9	88.0	103.6	283.0
MODIS	SIO	15.7	66.7	1.3	64.1	270.1	342.4	73.5	261.4
	SPG	16.3	90.0	1.2	64.8	125.2	343.1	71.0	260.9
AATSR	SIO	26.5	65.2	2.0	55.2	33.0	87.8	2.3	357.1
	SPG	27.1	66.2	1.0	55.3	33.3	86.6	3.9	355.7
ATSR2	SIO	22.8	60.2	2.3	55.2	28.9	81.7	3.6	300.4
	SPG	23.3	62.9	1.3	55.2	29.0	80.4	8.7	300.7

The range of data variability used to build the tables reported in the tables below:

Table 9: Range of variation of 6SV variables

Sensor	Site	SZA min	SZA max	Step	VZA min	VZA max	Step	Relative Azimuth Angle min	Relative Azimuth Angle min max	Relative Azimuth Angle Step
PARASOL	SIO	15	72	3	15	72	3	150	180	3
MERIS	SIO	15	72	3	15	72	3	150	180	3
MODIS	SIO	15	72	3	15	72	3	150	180	3
AATSR	SIO	15	72	3	15	72	3	150	180	3
ATSR2	SIO	15	72	3	15	72	3	150	180	3

This document is the property of Magellium. It cannot be reproduced, nor communicated without written permission.

Table 10: Range of variation of wind speed variables

	Range	Step	Number of values
Wind speed	[0 – 10] m/s	0.5 m/s	11

3.2.4 Ancillary data

Water vapour content and ozone content are taken from the ERA interim datasets. ERA-Interim is a global atmospheric reanalysis from 1979 to present. Global atmospheric and surface parameters from 1 January 1979 to present, at T255 spectral resolution (~80 km) on 60 vertical levels are available. For this study, 6-hourly atmospheric fields on water vapour content, ozone content, and wins speed have been downloaded from 2001 to year 2012 from the ECMWF Data Server.

Table 11: Ancillary data needed in the Sunglint method

Data	Source
Water vapour content	ECMWF ERA Interim
Ozone content	ECMWF ERA Interim
Wind speed	Retrieved from process

This document is the property of Magellium. It cannot be reproduced, nor communicated without written permission.

4 Dataset analysis to monitor the sensor radiometry using sunglint

4.1 Introduction

This section provides the results of the method set up to estimate the change in the radiometry over sunglint target. The results are provided for all sensors for which sunglint has been identified in the temporal series of acquisitions available in the database. Only data available over SIO site have been processed. The details of the implementation are provided for the processing of one single acquisition. Then, the results are provided for the processing of the data time series

4.2 Site selection

Sunglint is not related to a site since it is only an effect observed in specific solar and view geometries. In consequence, the sunglint target has been searched in the large available datasets of DIMITRI database in data acquired over SIO and SPG sites according pixel selection set in the method.

The two site locations are reported in the following table. Sunglint spot is searched inside the acquisitions which contains these two sites.

Table 12: Ocean site location

Site name	Location	Illustration
South Pacific Gyre	[-30.5 S, -31.0 S, -129.0 W, -129.5 W]	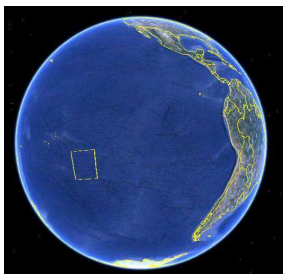
South Indian Ocean	[-30.0 S, -30.5.0 S, 80.0 E, 80.50 E]	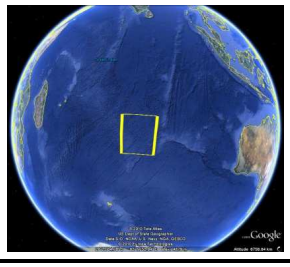

This document is the property of Magellium. It cannot be reproduced, nor communicated without written permission.

4.3 Data selection

The dataset analysis aims to identify the acquisitions which will be suitable to apply the method. The data selection aims to find sun glint target inside the acquisition based on the following criterion:

$$\theta_n < 4°$$

The selection of pixels acquired in the sunglint area is performed on each acquisition. The selection is done at the ingestion level. The following table reports the number of acquisitions of the database available for the radiometry monitoring using sunglint, for the two sites respectively and each sensor.

4.4 Analysis of MODIS

4.4.1 Over SIO

4.4.1.1 Details of results for a single date

The following results and illustrations detail the estimation of the reflectance ratio for one date: MODIS acquisition of 07/01/2010 which shows large clear area located in the sunglint. The illustration follows the implementation plan description in the previous section, step by step.

Read the database and select images acquired in the sunglint spot.

This document is the property of Magellium. It cannot be reproduced, nor communicated without written permission.

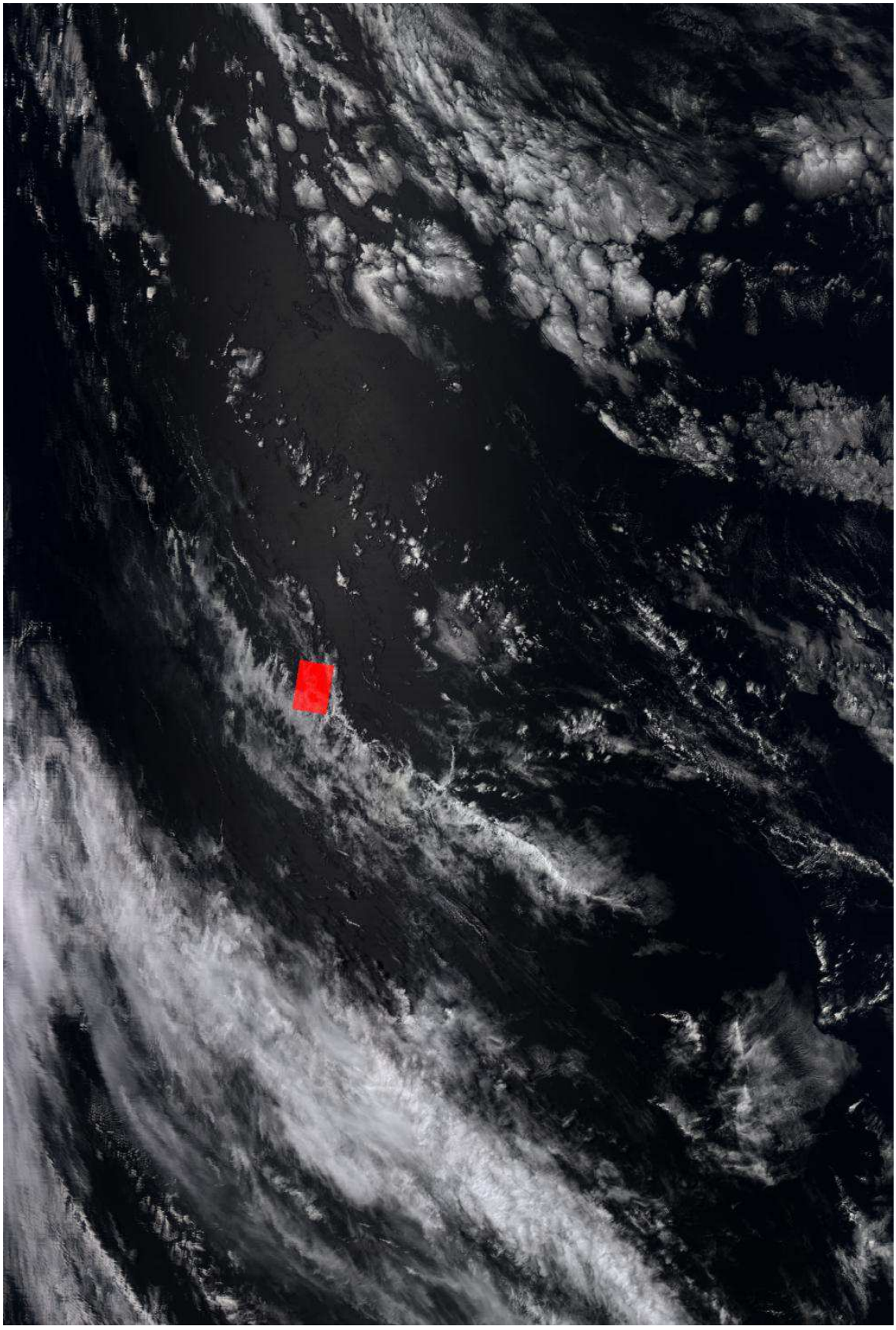

Figure 7: MODIS acquisition 07/01/2010 (Product MYD021KM.A2010007.0820.005.2010008134354.gscs_000500561122_hdf)

This document is the property of Magellium. It cannot be reproduced, nor communicated without written permission.

Read the TOA reflectances of clear pixels acquired into the site footprint for the selected date.

The TOA reflectances of this acquisition are represented in the figure below for channels 1 to 8, and 2. This acquisition is cloudy, but large areas centered in the middle of the acquisition indicate the presence of the sunglint in a more or less contrasted way.

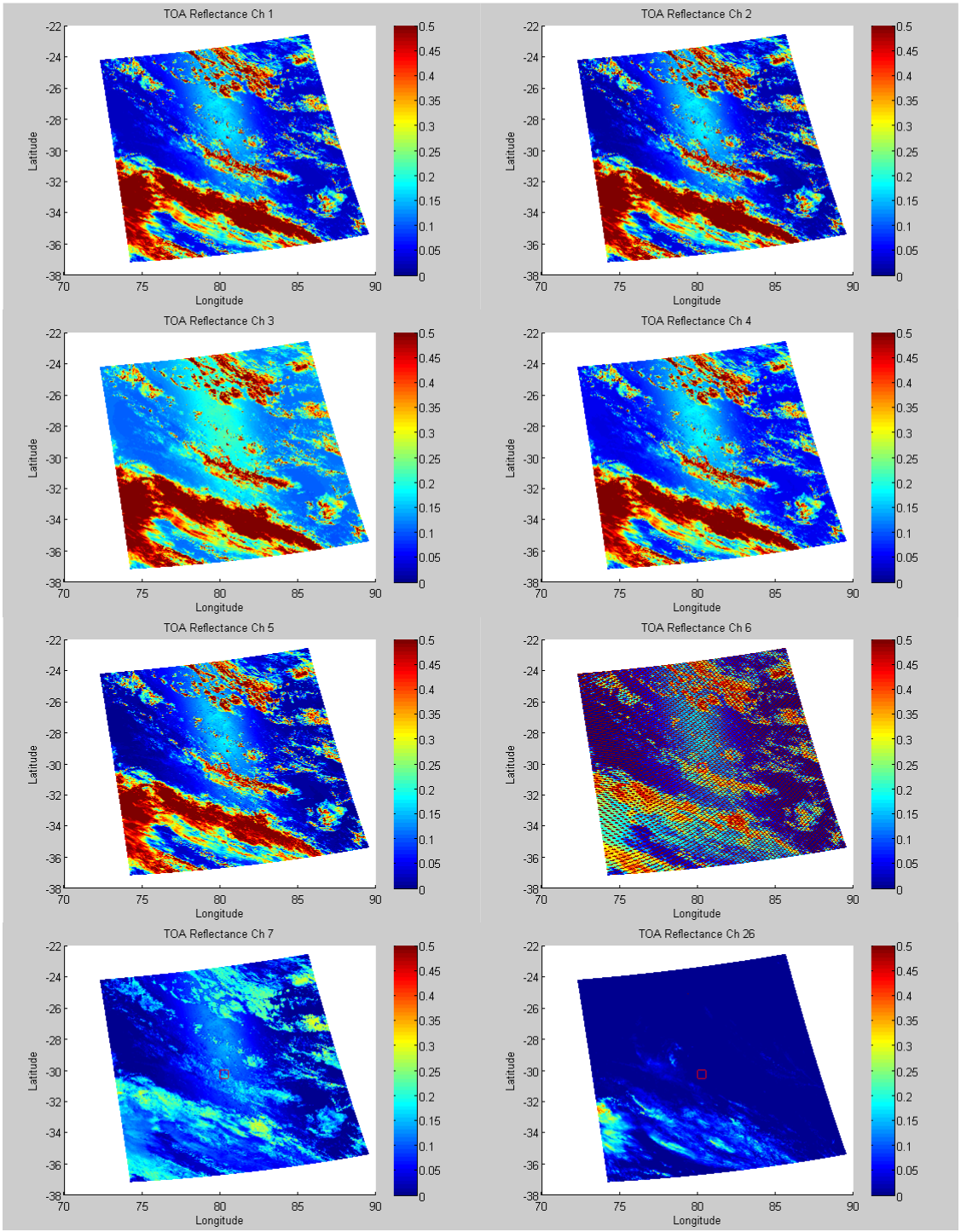

Figure 8: TOA reflectances in MODIS Reflected Solar bands 1-7, 26

In order to identify the region of interest which contains the sunglint spot, the computation of the wave angle is performed. It provides a mask of the selected area where the sunglint

This document is the property of Magellium. It cannot be reproduced, nor communicated without written permission.

method could be used if all conditions are met. The mask is represented in the figure below. The SIO site location is represented by a red square.

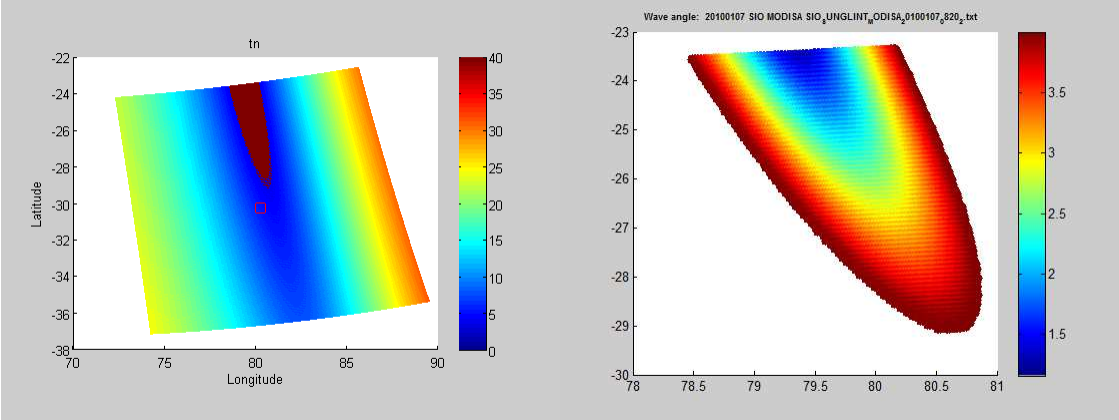

Figure 9: Wave angle for the acquisition (left). Zoom inside the selected sunglint (right) area. Geographic representation.

Based on the mask use, the pixels belonging to the selected area are extracted from the full acquisition.

The TOA reflectance in the VIS and NIR channel (1 and 2) are represented below. This representation is shown in image coordinates (Column/Row).

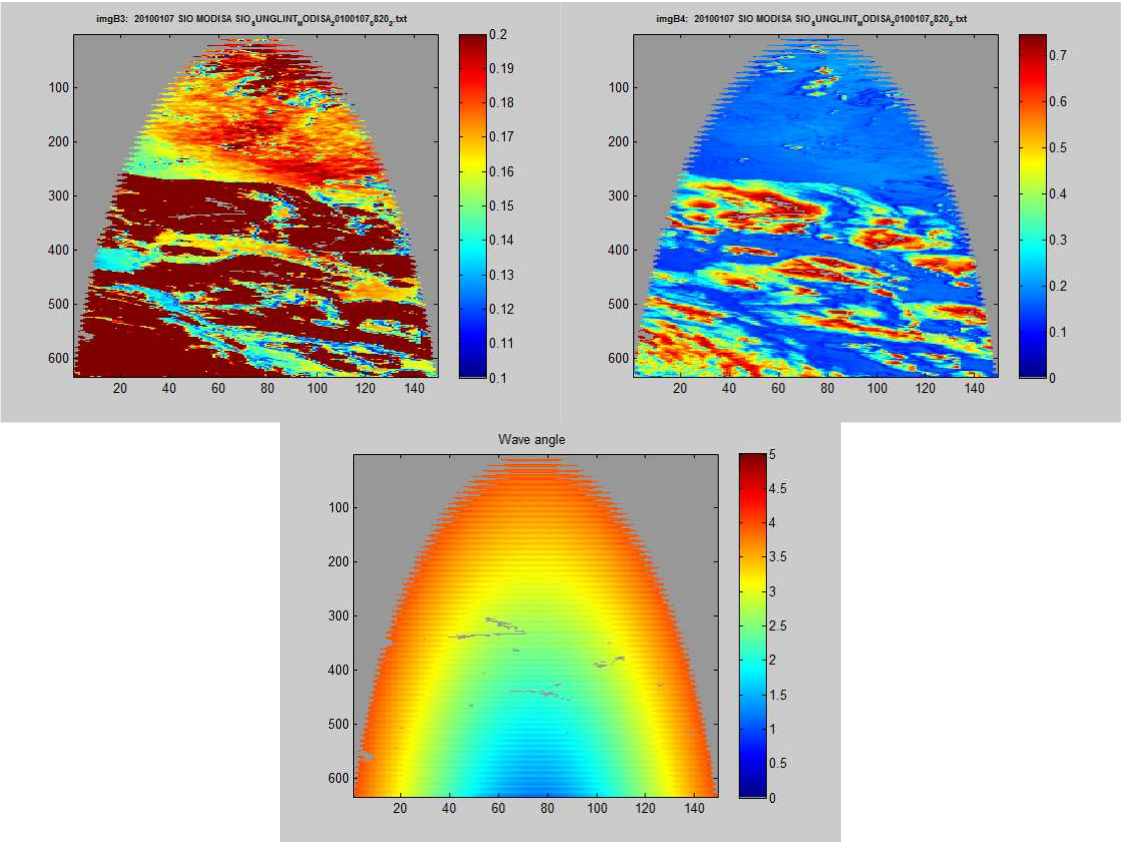

Figure 10: TOA reflectances in channels 1 and 2, and wave angle

This document is the property of Magellium. It cannot be reproduced, nor communicated without written permission.

Read auxiliary data

Wind speed, Water vapor content, and Ozone content are extracted from ERA datasets in the sunglint area. The images of these variables are represented hereafter.

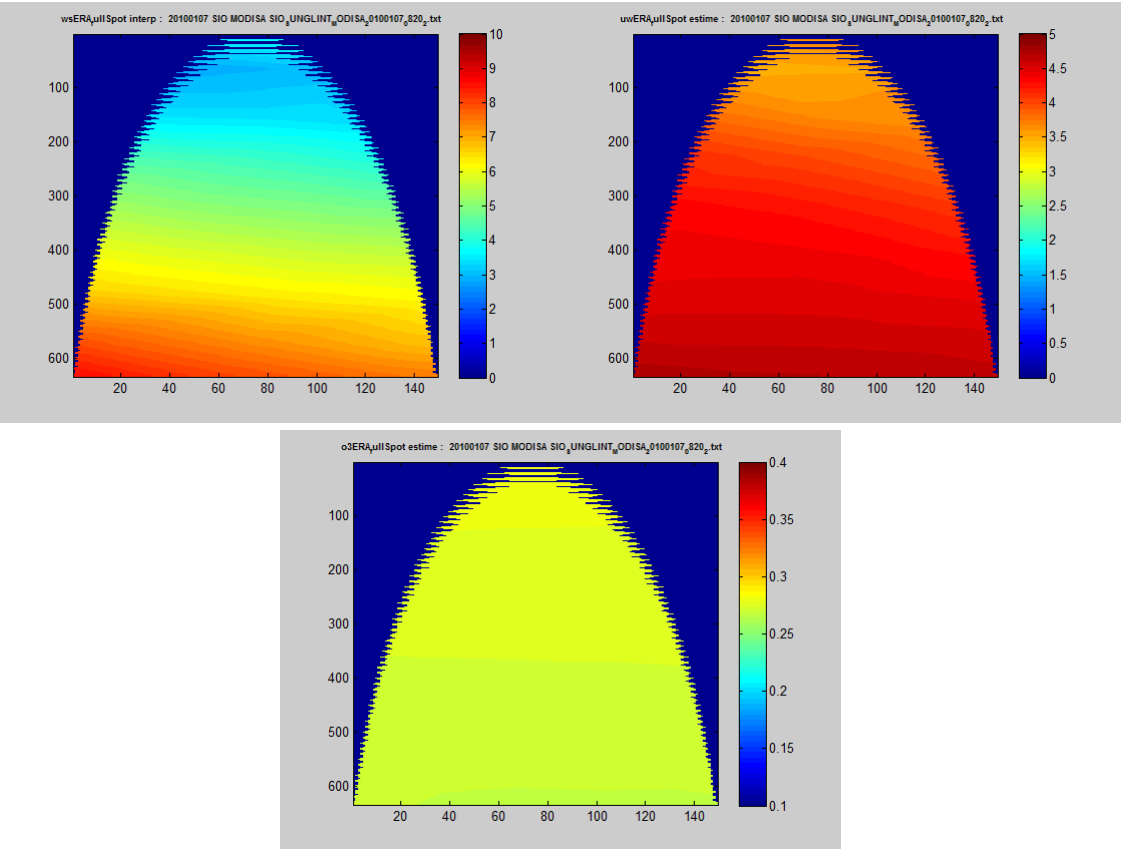

Figure 11: Windspeed (m/s), Water vapour content (g/cm2) and ozone content (cm.atm) in the sunglint spot.

The sunglint area is a large area, around 1.5 x 6 degrees. The variability of the data could be large, as it is observed in particular for the wind speed, for which a latitudinal gradient is observed, with wind speed varying from 3 to 10m/s. A mean level of ozone content around 0.28 cm.atm is observed and a water vapor gradient of 3 to 5 g/cm2 is also observed.

Note that wind speed is extracted as an indicator but is not used in the method.

Check Pixels selection test

- Select valid pixels
- Select clear pixels
- Select NIR TOA pixels such as ρNIR > 0.15

A mask of valid pixel is applied is computed from the acquisition. These data are flagged inside the products, and the information is conserved in the data extracted from the ingestion module. For MODIS acquisitions, the main channel which contains INVALID data is the SWIR (1.6µm) channel, as it can be seen in Figure 7, but it happened that some saturation or other problem exists. These data are removed of the selected pixels by the pixel selection module. The mask is represented hereafter.

This document is the property of Magellium. It cannot be reproduced, nor communicated without written permission.

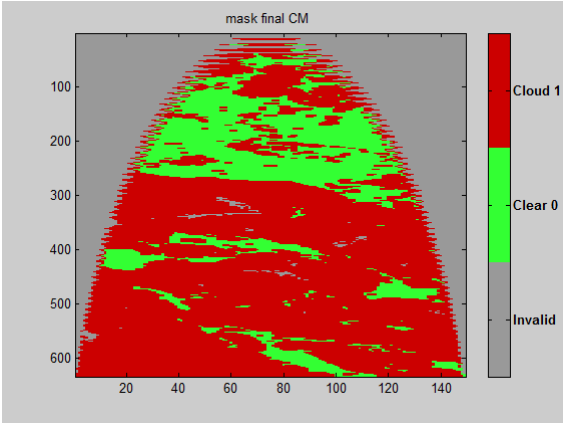

Figure 12: Cloud mask

Correct TOA reflectances from gaseous absorption

The comparison of TOA measurements to the simulation is performed on TOA reflectance normalized to gaseous absorption.

The SMAC method allows to estimate the gaseous transmission for the atmospheric content read from ERA data at the date of acquisition. These coefficients are provided for each spectral bands used in the method.

Estimate wind speed in the reference band

The wind speed is derived based on a LUT of TOA reflectances generated with 6SV, for various wind speed. The wind speed value is selected such as the TOA reflectance measured agrees best with the modelled one.

This step is controlled using a scatterplot of TOA reflectance measured versus estimated. Any point diverging from the 1:1 line indicates a problem in the wind speed value retrieval.

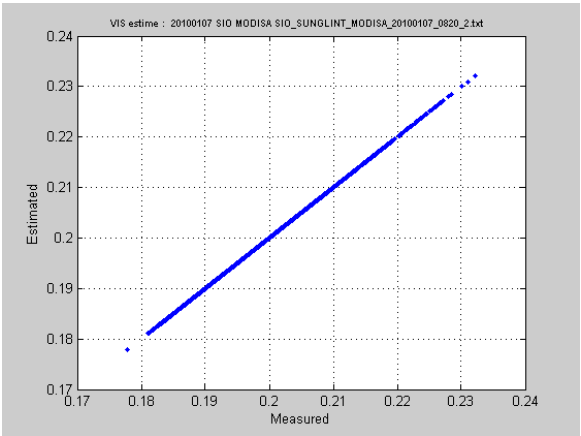

Figure 13: Control of the windspeed retrieval

The wind speed estimated using the LUT is analysed and only pixels for which wind speed is lower than 5m/s are kept.

For this acquisition, the histogram of the retrieved wind speed is represented hereafter.

This document is the property of Magellium. It cannot be reproduced, nor communicated without written permission.

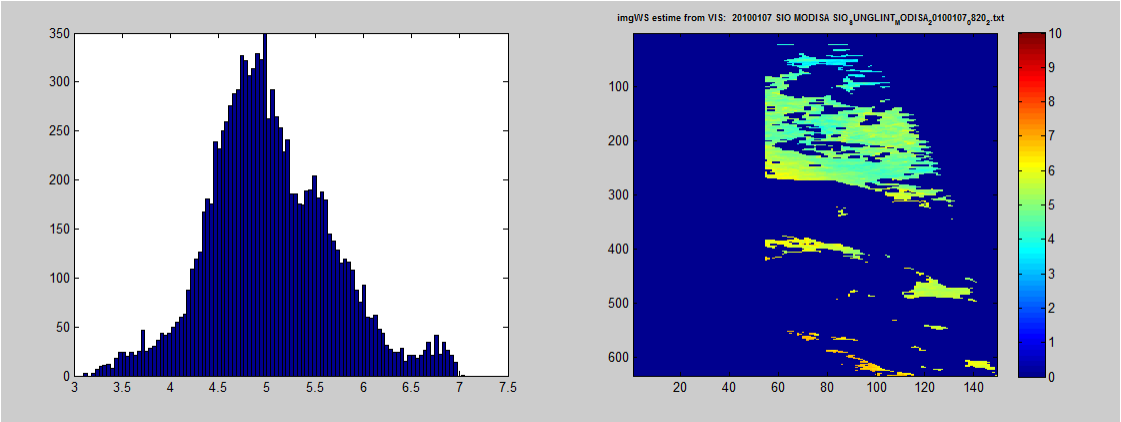

Figure 14: Estimated wind speed

Due to a limited LUT in view zenith angle range, simulation for θs < 20° is not possible using this version.

The difference between ERA and estimated wind speed is represented on the following graph. The difference is depending on the location but as expected, the largest difference occurs for small wind speed.

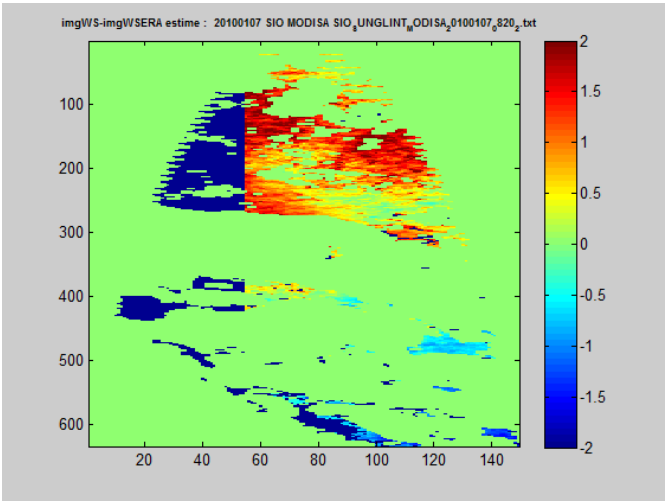

Figure 15: Difference between ERA wind speed and estimated wind speed

Estimate the TOA reflectance in the bands to be calibrated using estimated wind speed

Once the wind speed estimated, it is used to simulate the TOA reflectances in the other channels.

The ratio of measured to estimated reflectance is computed for all the pixels selected in the area. The scatterplot is shown hereafter for the three bands, BLUE, NIR and SWIR.

5814 pixels have been selected in the acquisition. However, there are fewer pixels processed in the SWIR band because there are a lot of invalid flagged data in this channel.

The dynamic of the sunglint reflectance range is around 5% from the lowest to the highest reflectance in the three channels. Statistics results are provided in the scatterplot figures. The correlation is good for the NIR band (0.9993), and the scattering is low. The coefficient correlation is 0.09046 in the BLUE channel and 0.9523 in the SWIR channel.

This document is the property of Magellium. It cannot be reproduced, nor communicated without written permission.

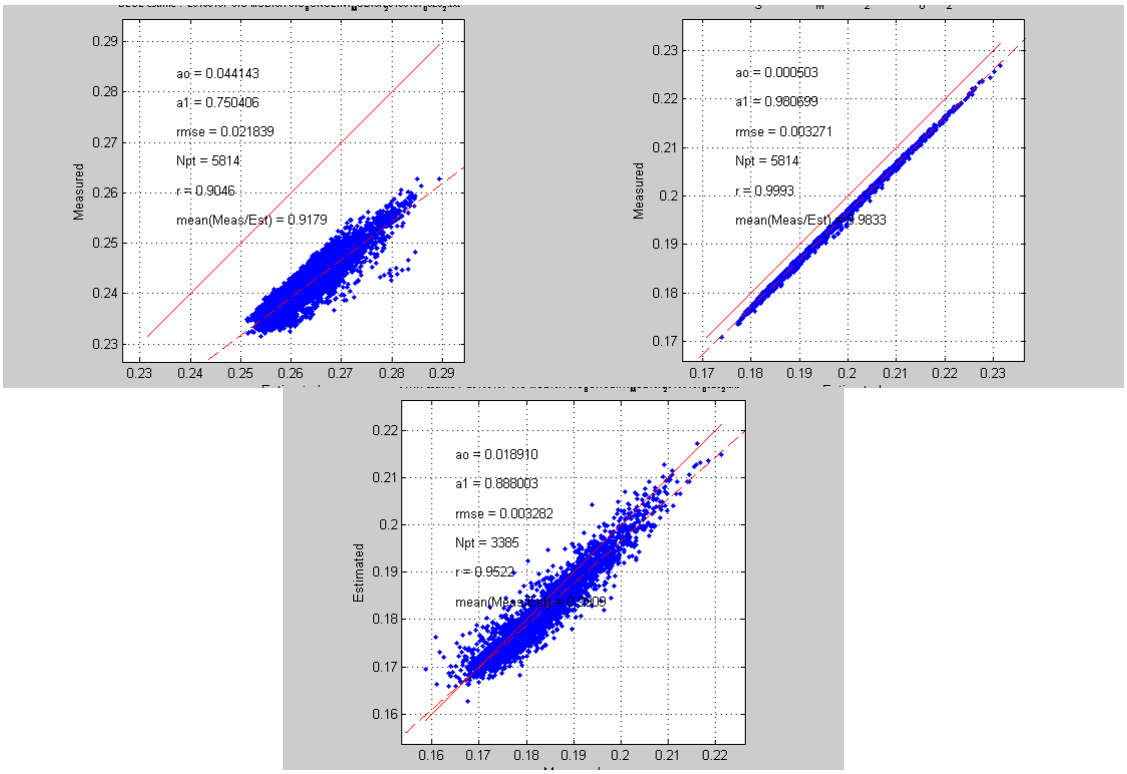

Figure 16: Scatterplot of simulated TOA reflectances versus measured TOA reflectances

The spatial variability of the measured and simulated reflectances in the NIR channel is represented in the images below, together with the difference between the two maps. The highest difference is located in the top of the image.

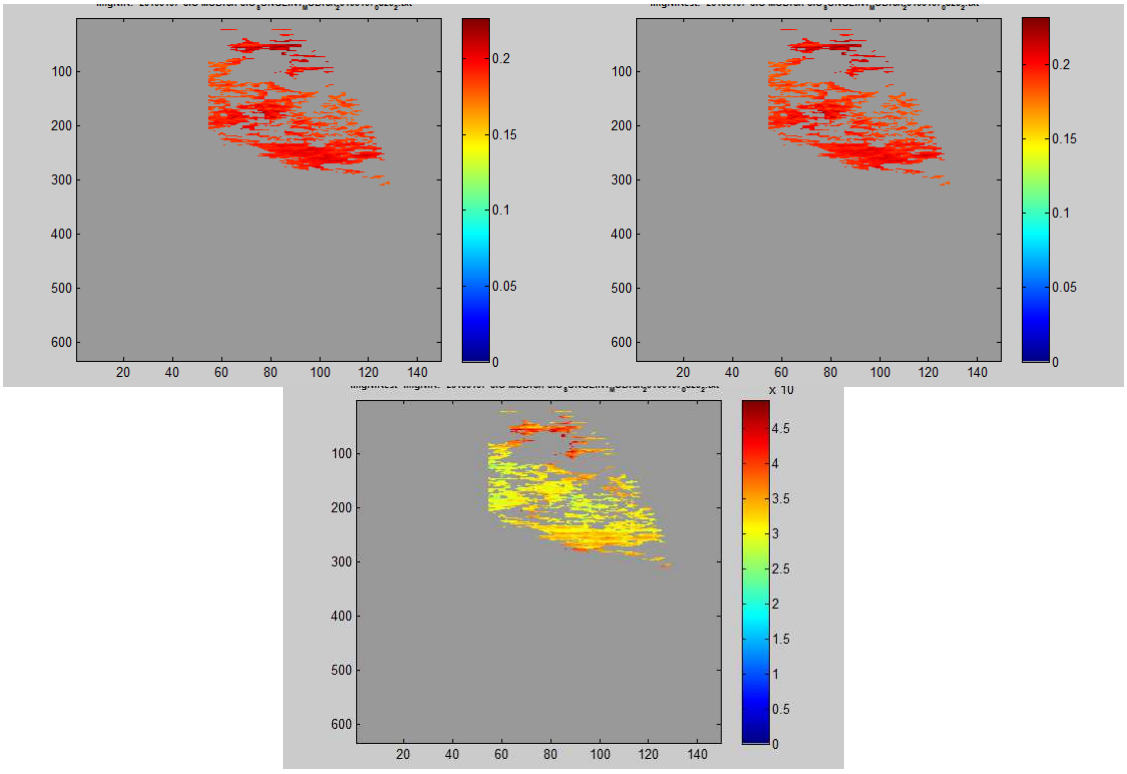

Figure 17: TOA reflectance in the NIR. Measured (top left), Simulated (top right), difference estimated minus measured (bottom).

This document is the property of Magellium. It cannot be reproduced, nor communicated without written permission.

At this step, an analysis is also performed to check that no correlation is observed between the reflectance ratio and the estimated wind speed. The figure below shows the distribution of the ratio versus the estimated wind speed.

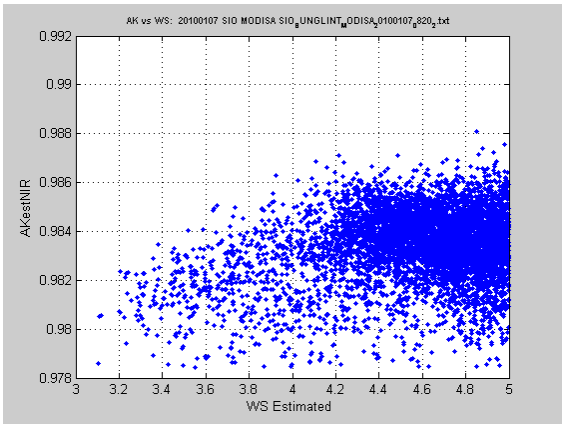

Figure 18: Measured to Simulated TOA reflectance ratio in the NIR versus estimated wind speed

Estimate the measured to simulated TOA reflectance ratio in the BLUE, NIR, and SWIR bands

Once the simulated TOA reflectance estimated all the valid pixels, a map of the ratio is computed allowing to see the spatial variability and possible effects due to cloud edge. As an example, the map of reflectance ratio in the NIR channel is represented here after:

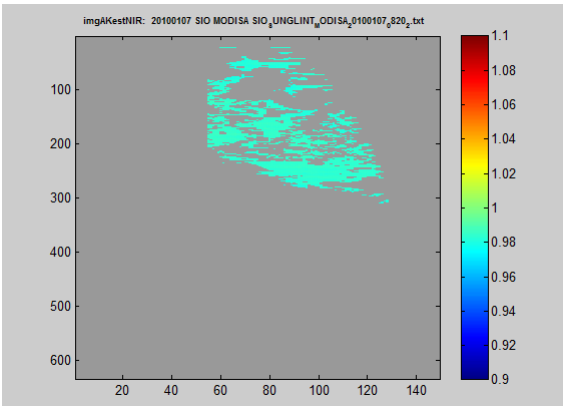

Figure 19: Map of Ak in the NIR band

The histograms of the ratio in the three bands are the following:

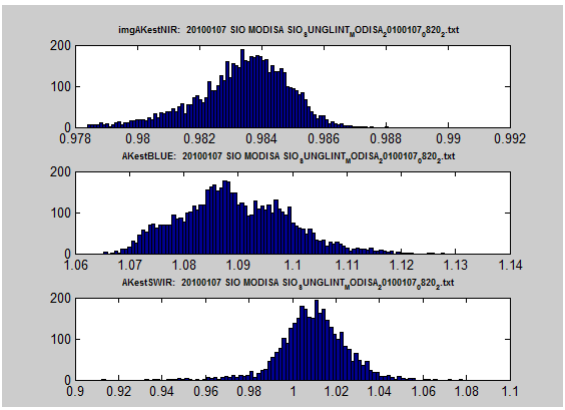

Figure 20: Ratio of Measured to Simulated TOA reflectance histograms

This document is the property of Magellium. It cannot be reproduced, nor communicated without written permission.

4.4.1.2 Multiyear results

The change in sensor radiometry is estimated by computing the mean of the measured to simulated TOA reflectances ratio for all available acquisitions (Eq. 19). It is represented for the three bands in the figures below. Sunglint is present mainly in the acquisition of December and January month. This is the reason why there some discontinuities between years.

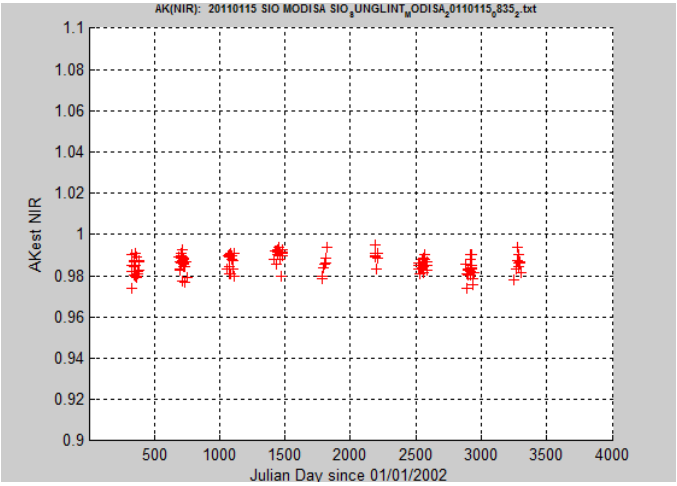

Figure 21: Temporal variability of mean ratio between 2002 and 2011 – NIR band

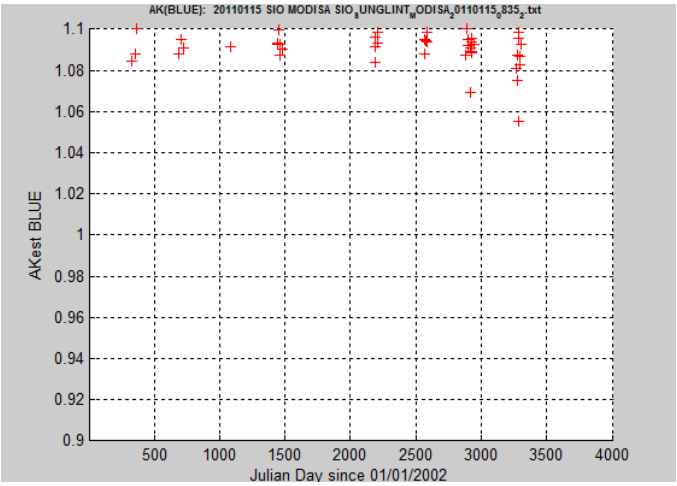

Figure 22: Temporal acquisition of mean ratio between 2002 and 2011 – BLUE band

This document is the property of Magellium. It cannot be reproduced, nor communicated without written permission.

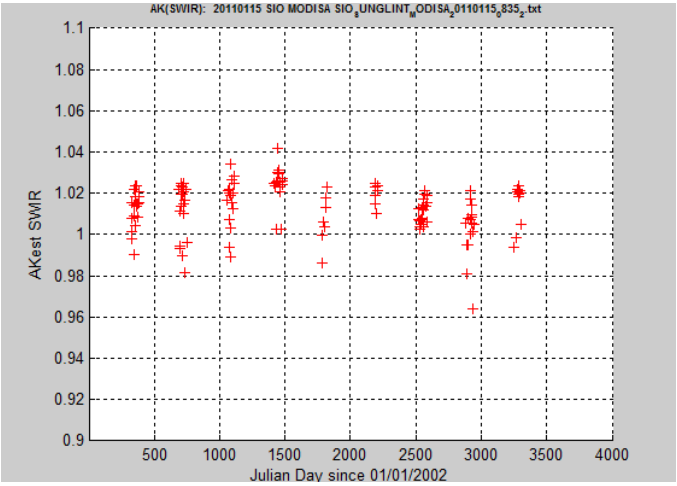

Figure 23: Temporal acquisition of mean ratio between 2002 and 2011 – SWIR band

The mean ratio in the NIR seems to be stable between 0.98 and 1. In the blue, there is some variability, with a ratio around 1.1. Outliers have not been removed.

The variability in the SWIR is higher than in the NIR. Outliers have not been removed.

This document is the property of Magellium. It cannot be reproduced, nor communicated without written permission.

4.5 Analysis of MERIS

4.5.1 Over SIO

4.5.1.1 Details of results for a single date

The following results and illustrations detail the estimation of the reflectance ratio for one date: MERIS acquisition of 23/11/2008 which shows large clear area located in the sunglint. The illustration follows the implementation plan description in the previous section.

Read the database and select images acquired in the sunglint spot.

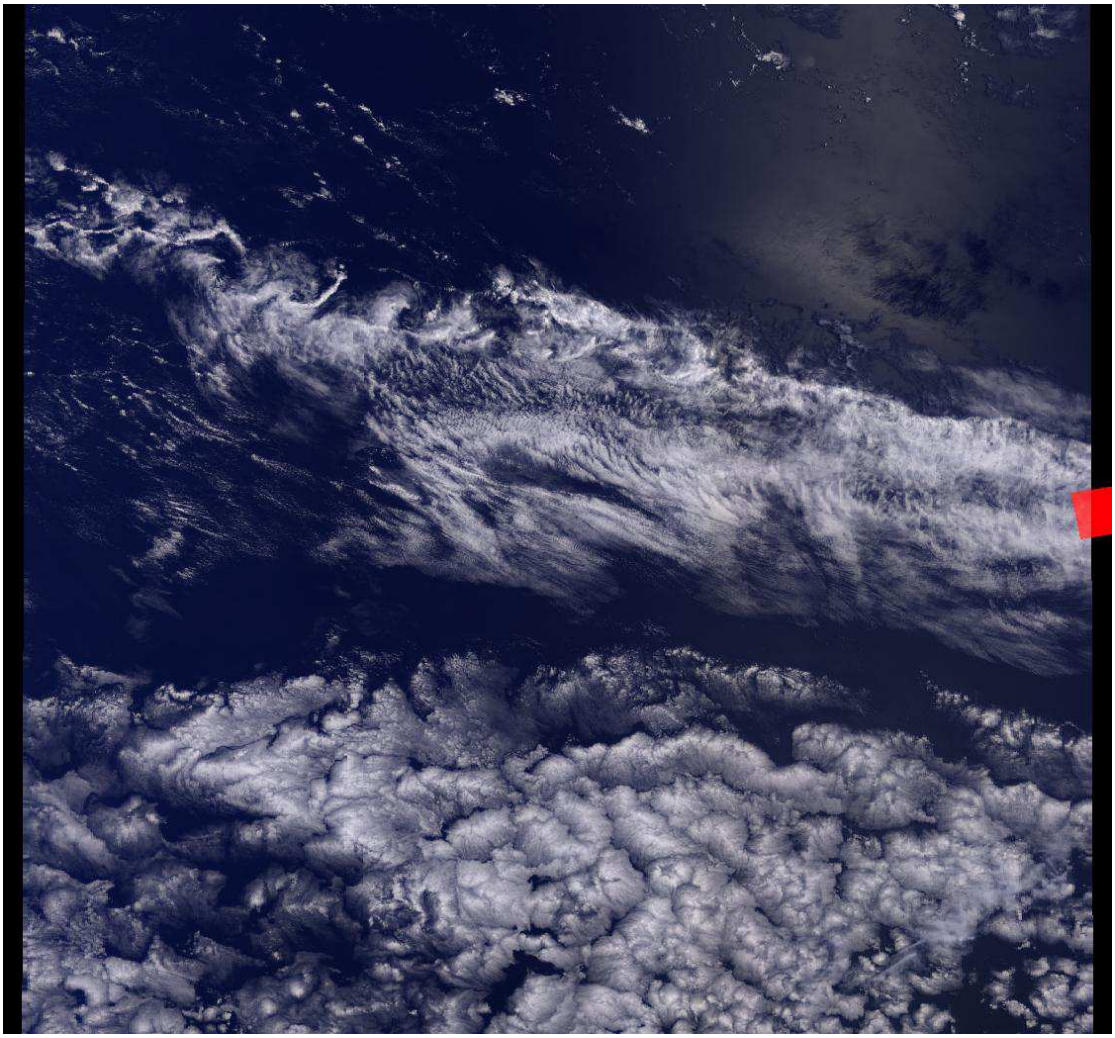

Figure 24: MERIS acquisition 23/11/2008 (Product MER_RR__1PRMAP20081123_044118_000001832074_00076_35200_0001_N1)

Read the TOA reflectances of clear pixels acquired into the site footprint for the selected date.

The TOA reflectances of this acquisition are represented in the figure below for the NIR channels. The spot has a large area which has a lowest level of reflectance than the rest of the

This document is the property of Magellium. It cannot be reproduced, nor communicated without written permission.

images, probably due to a cloud shadow. Large areas centered in the middle of the acquisition indicate the presence of the sunglint in a more or less contrasted way.

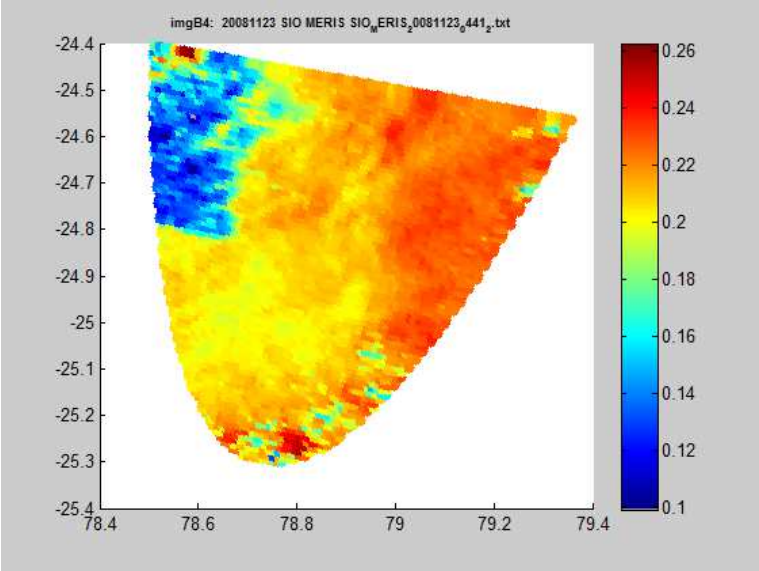

Figure 25: TOA reflectances in MERIS Reflected Solar bands 13

The computation of the wave angle is performed to provide a mask of the selected area where the sunglint method could be used if all conditions are met.

The mask is represented in the figure below.

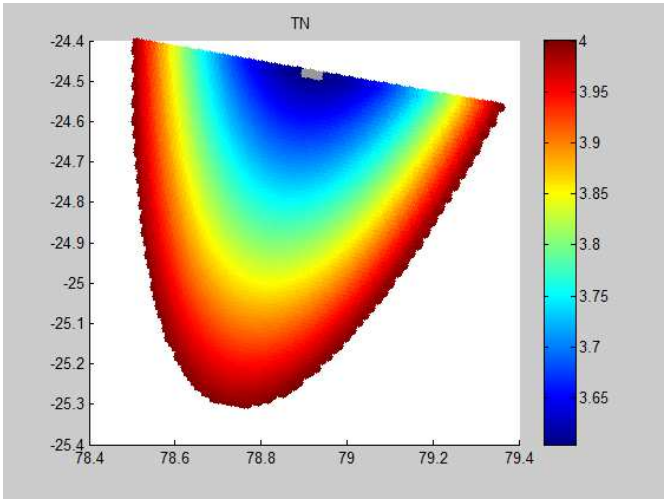

Figure 26: Wave angle inside the sunglint area

Based on the mask use, the pixels belonging to the selected area are extracted.

This document is the property of Magellium. It cannot be reproduced, nor communicated without written permission.

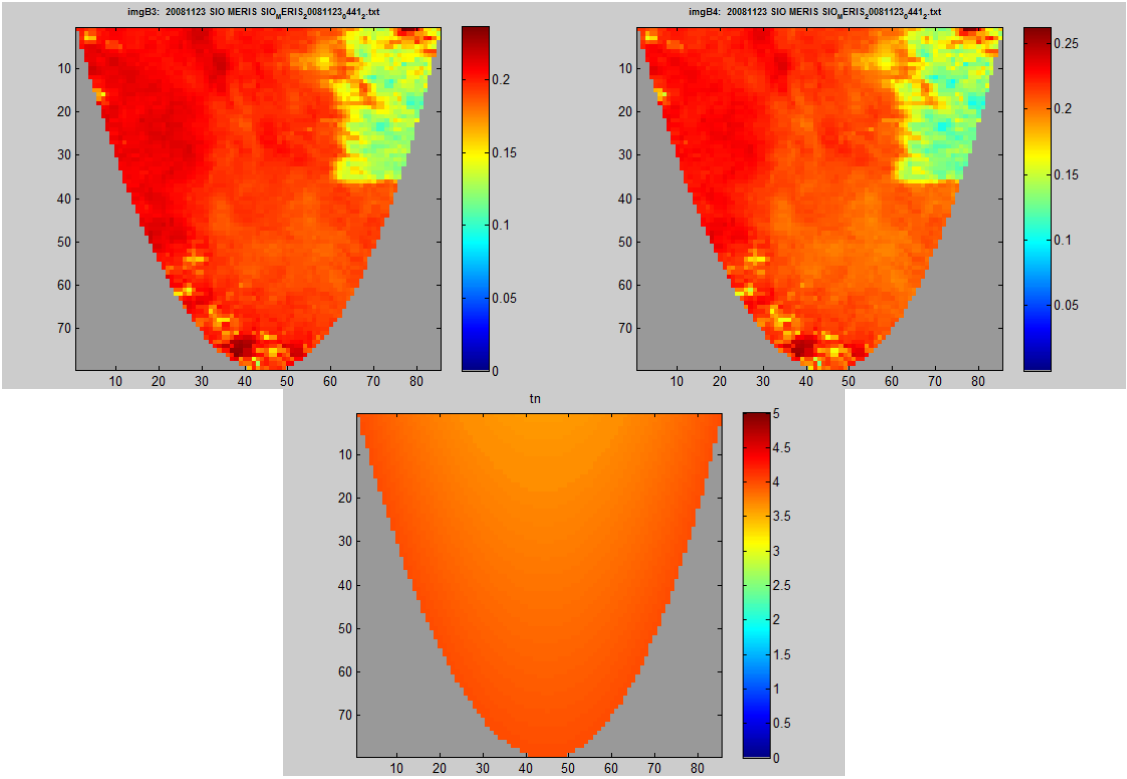

Figure 27: TOA reflectances in channels 7 and 13, and wave angle

Read auxiliary data

Wind speed, Water vapor content, and Ozone content are extracted from ERA datasets in the sunglint area.

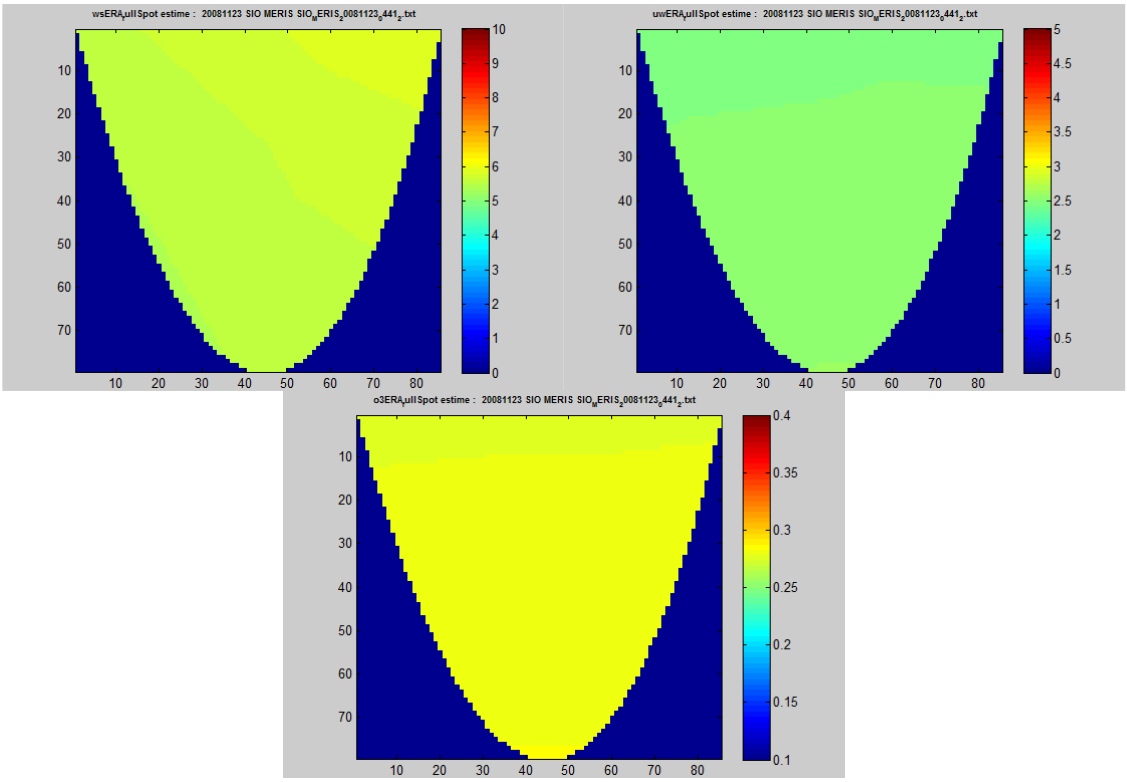

Figure 28: Windspeed, Water vapour content and ozone content

This document is the property of Magellium. It cannot be reproduced, nor communicated without written permission.

The sunglint area is a large area, around 1.5 x 2.5 degrees. The variability of the data for this date is low. Wind speed varies between 5 and 6 m/s. A mean level of ozone content around 0.28 cm.atm is observed and a water vapor is around 2.4 g/cm2.

Check Pixels selection test

- Select valid pixels
- Select clear pixels
- Select NIR TOA pixels such as ρNIR > 0.15

A mask of valid pixel is applied is computed from the acquisition. These data are flagged inside the products, and the information is conserved in the data extracted from the ingestion module.

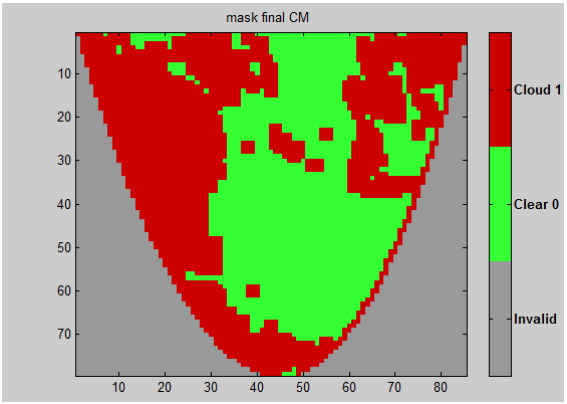

Figure 29: Cloud mask

Correct TOA reflectances from gaseous absorption

The comparison of TOA measurements to the simulation is performed on TOA reflectance normalized to gaseous absorption.

The SMAC method allows to estimate the gaseous transmission for the atmospheric content read from ERA data at the date of acquisition. These coefficients are provided for each spectral bands used in the method.

Estimate wind speed in the reference band

The wind speed is derived based on a LUT of TOA reflectances generated with 6SV, for various wind speed. The wind speed value is selected such as the TOA reflectance measured agrees best with the modelled one.

This step is controlled using a scatterplot of TOA reflectance measured versus estimated. Any point diverging from the 1:1 line indicates a problem in the wind speed retrieval.

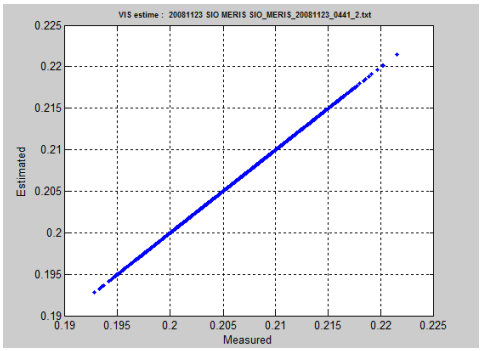

Figure 30: Control of the windspeed retrieval

This document is the property of Magellium. It cannot be reproduced, nor communicated without written permission.

The wind speed estimated using the LUT is analysed and only pixels for which wind speed is lower than 5m/s are kept.

For this acquisition, the histogram of the retrieved wind speed is represented hereafter.

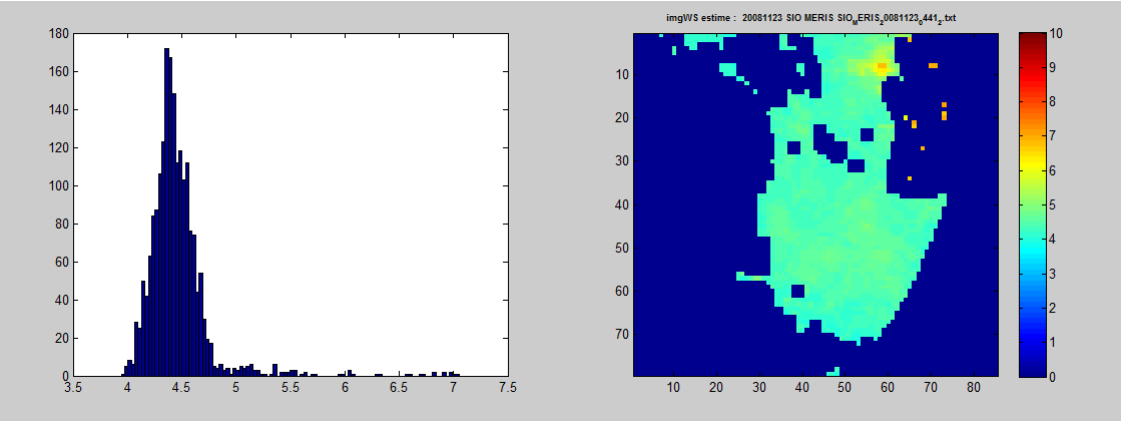

Figure 31: Estimated windspeed

The difference between ERA and estimated wind speed is represented on the following graph. The difference is depending on the location but as expected, the largest difference occurs for small wind speed.

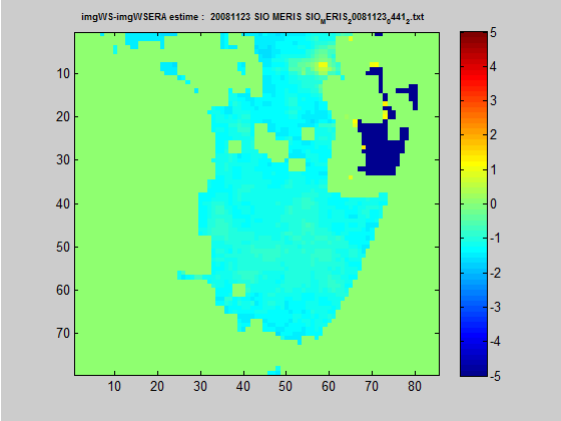

Figure 32: Difference between ERA wind speed and estimated wind speed

Estimate the TOA reflectance in the bands for which radiometry is monitored using estimated wind speed

Once the wind speed estimated, it is used to simulate the TOA reflectances in the other channels.

The ratio of measured to estimated reflectance is computed for all the pixels selected in the area. The scatterplot is shown hereafter for the two bands, BLUE, and NIR.

This document is the property of Magellium. It cannot be reproduced, nor communicated without written permission.

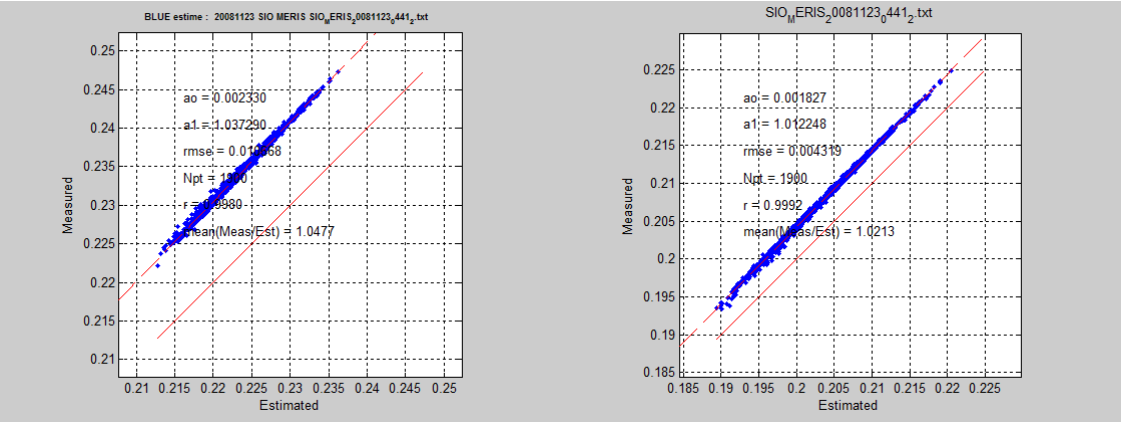

Figure 33: Scatterplot of simulated TOA reflectances versus measured TOA reflectances

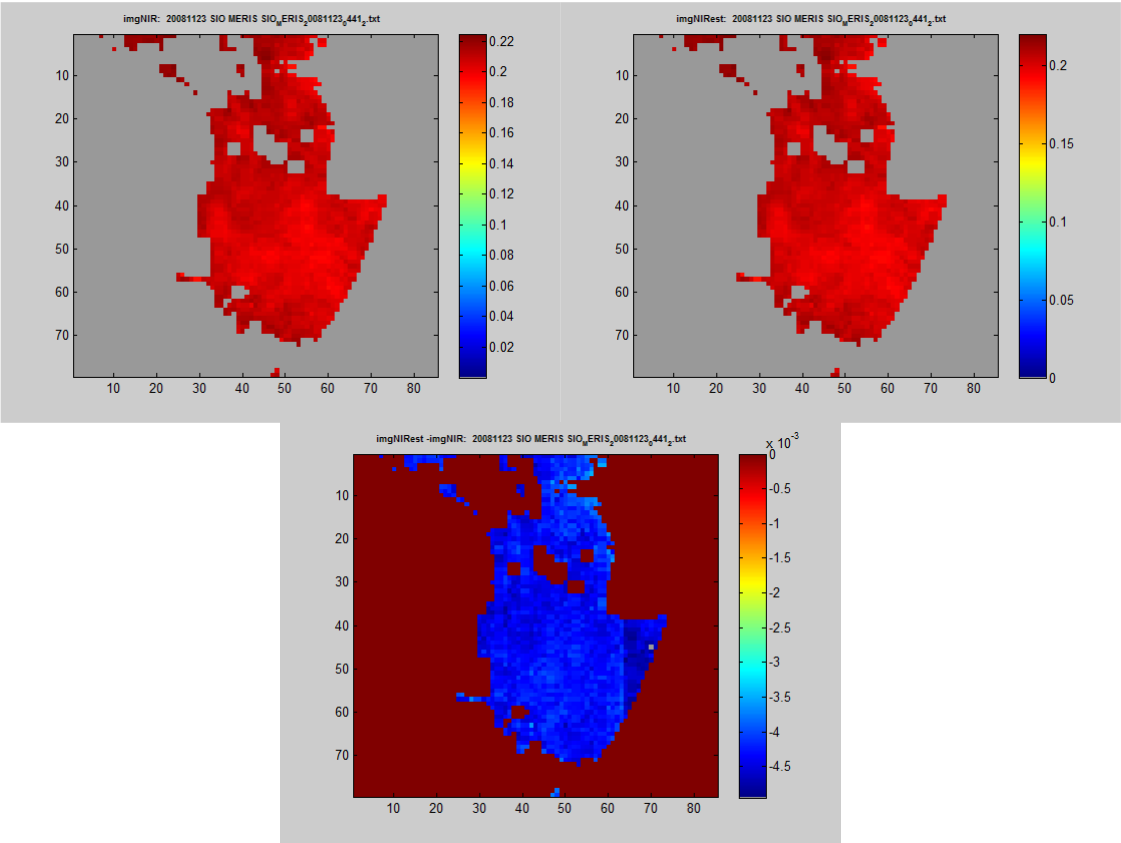

Figure 34: TOA reflectance in the NIR. Measured (top left), Simulated (top right), difference estimated minus measured bottom

At this step, an analysis is also performed to check that no correlation is observed between the reflectance ratio and the estimated wind speed.

This document is the property of Magellium. It cannot be reproduced, nor communicated without written permission.

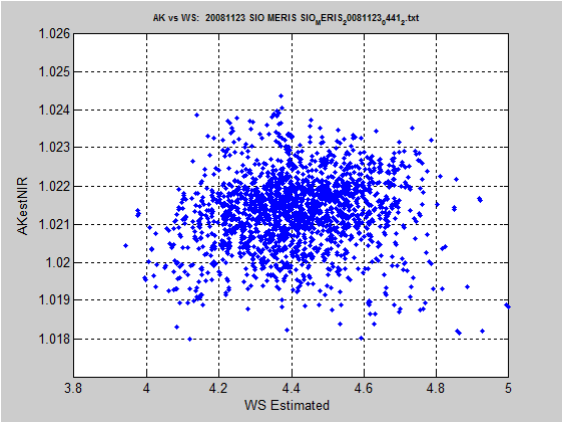

Figure 35: Measured to Simulated TOA reflectance ratio in the NIR versus estimated wind speed

Estimate the measured to simulated TOA reflectance ratio in the BLUE and NIR band

The map of reflectance ratio in the NIR channel is represented here after

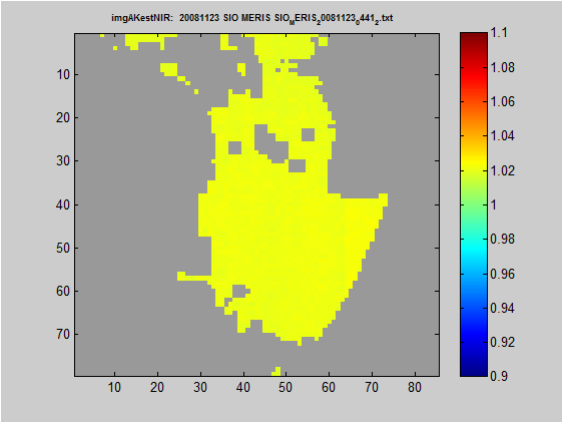

Figure 36: Map of Ak in the NIR band

The histograms of the ratio in the two bands are the following:

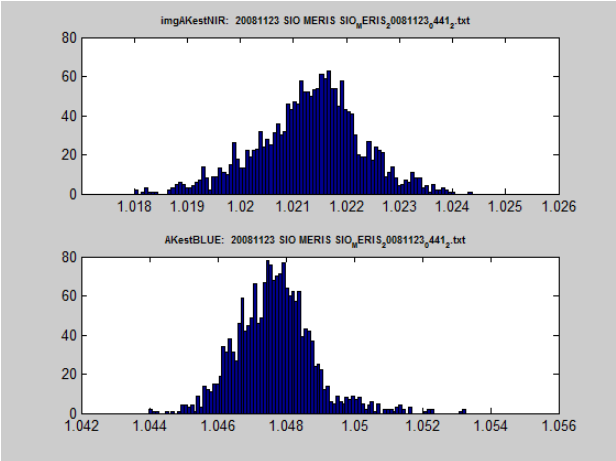

Figure 37: Reflectance ratio histograms

This document is the property of Magellium. It cannot be reproduced, nor communicated without written permission.

4.5.1.2 Multiyear results

The change in sensor radiometry is estimated by computing the mean of the measured to simulated TOA reflectances ratio for all available acquisitions (Eq. 19).

It is represented for the three bands in the figure below for all the acquisitions where Sunglint is present, i.e. mainly in the acquisition of December and January month. This is the reason why there some discontinuities between years.

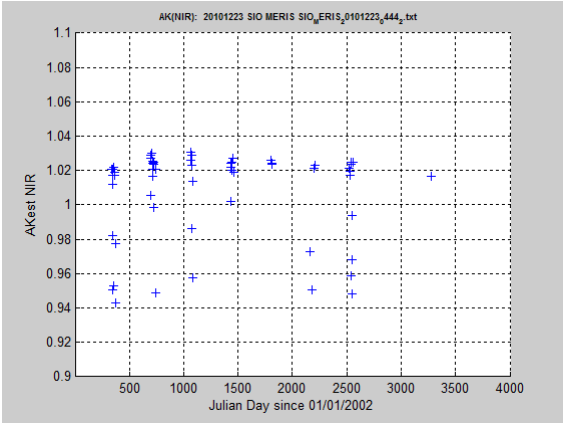

Figure 38: Temporal acquisition of mean ratio between 2002 and 2011 – NIR band

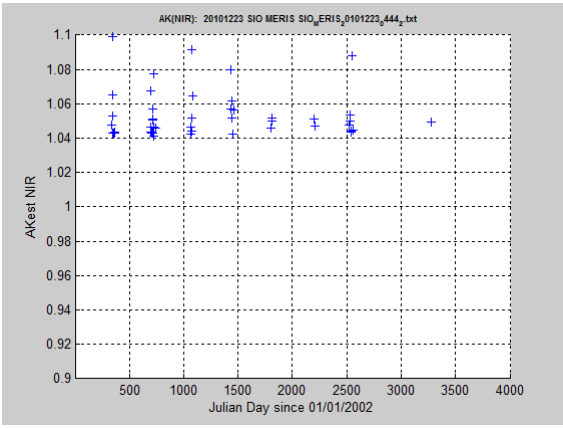

Figure 39: Temporal acquisition of mean ratio between 2002 and 2011 – BLUE band

This document is the property of Magellium. It cannot be reproduced, nor communicated without written permission.

4.6 Analysis of POLDER

4.6.1 Over SIO

4.6.1.1 Details of results for a single date

The following results and illustrations detail the estimation of the reflectance ratio for one date: PARASOL acquisition of 02/03/2011 which shows large clear area located in the sunglint. The illustration of the results follows the implementation plan description in the previous section. SIO site is represented by a red square in the quicklook.

Read the database and select images acquired in the sunglint spot.

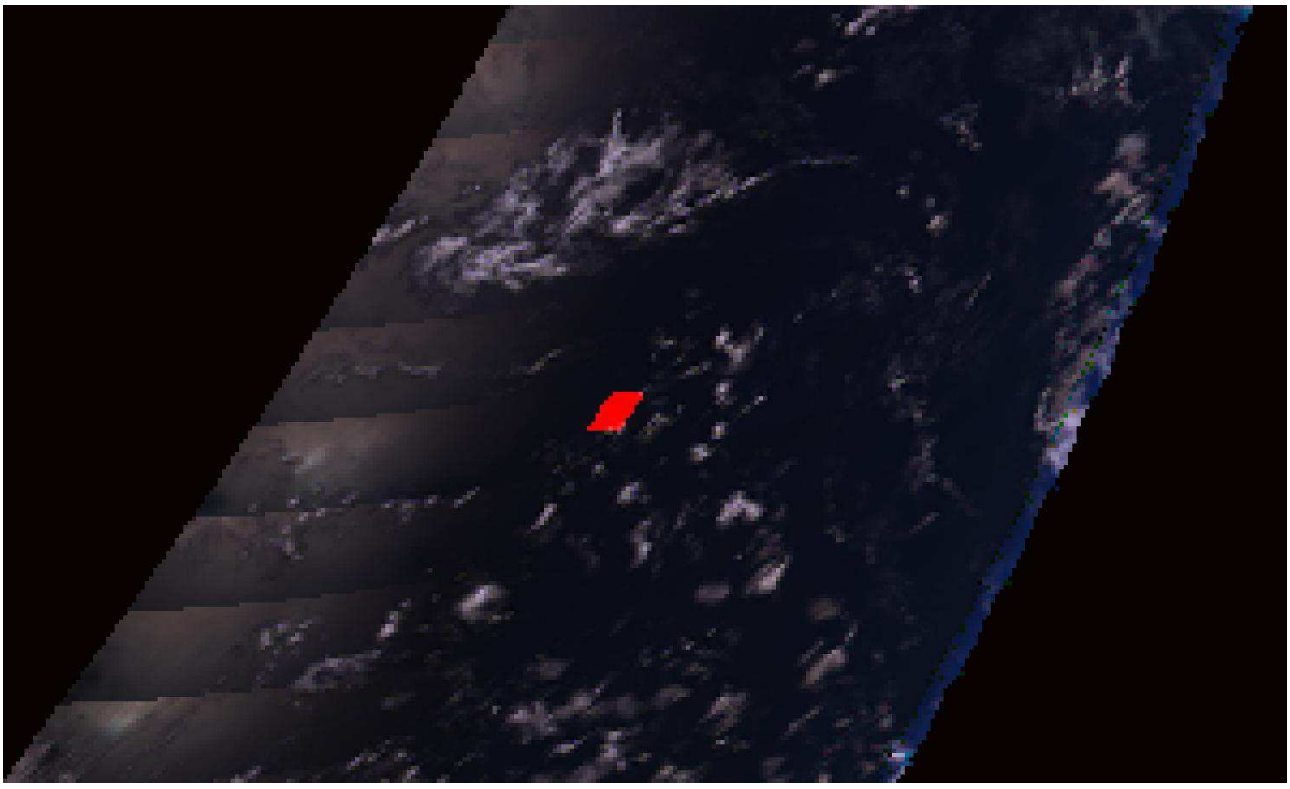

Figure 40: PARASOL acquisition 02/03/2011 (Product P3L1TBG1143099KD_s25_00_S35_00_e075_00_E110_00)

This document is the property of Magellium. It cannot be reproduced, nor communicated without written permission.

The acquisition sequence of the images is represented for the selected date here after. The sunglint spot appears on the left bottom of the images, then moved North with the satellite motion.

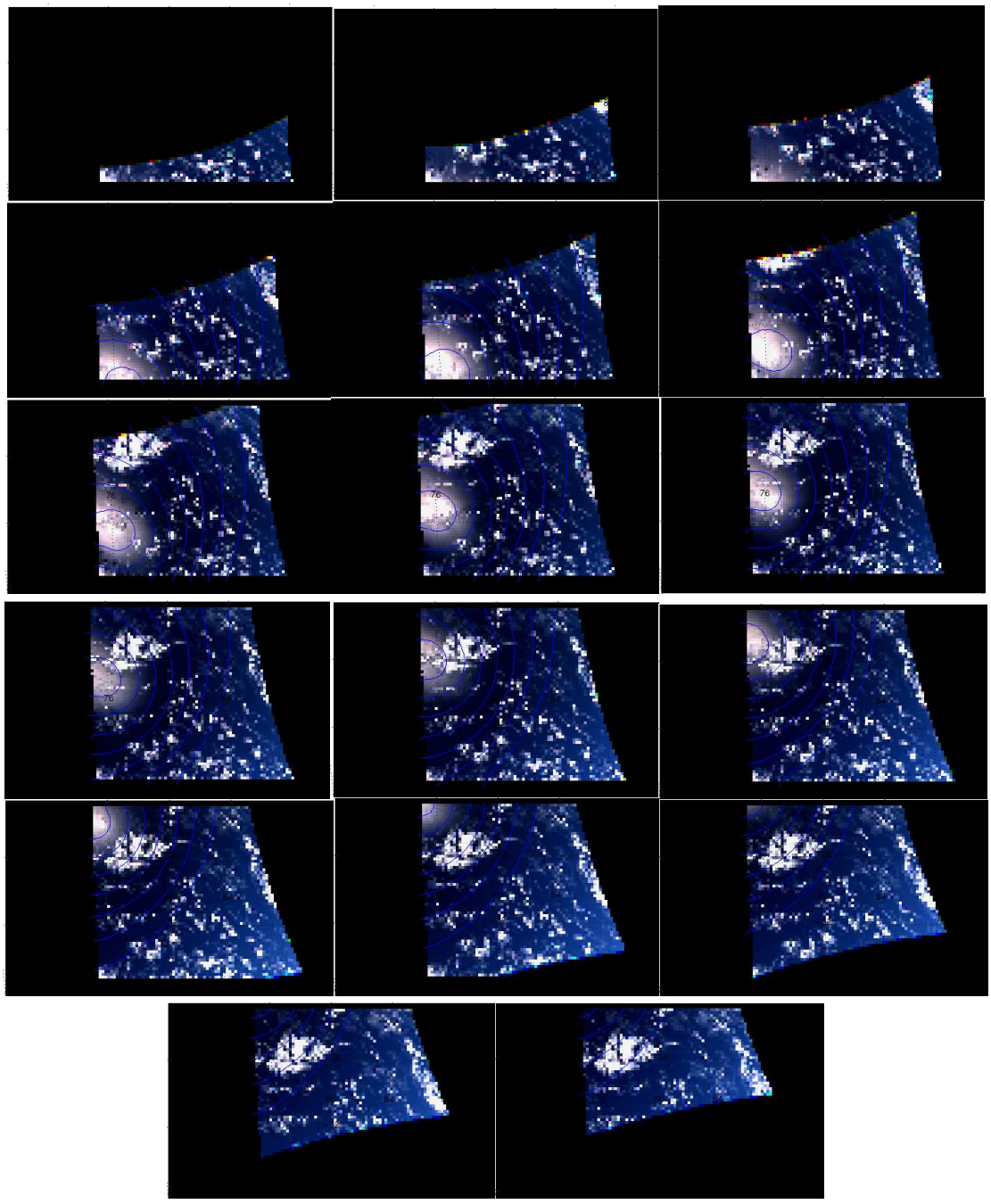

Figure 41: PARASOL image sequence containing the sunglint. Sequences are croissant from left to right.

This document is the property of Magellium. It cannot be reproduced, nor communicated without written permission.

Read the TOA reflectances of clear pixels acquired into the site footprint for the selected date.

The computation of the wave angle is performed to provide a mask of the selected area for each direction where the ratio could be estimated if all conditions are met.

Following the processes of the DIMITRI ingestion which processes data according the view direction, the representation of the data is illustrated for each direction, which is slightly different that the view in sequences shown before. For each direction, the wave angle, and the TOA reflectance in the NIR channel are represented hereafter.

Nb: In the following, the results are represented in Column/Row.

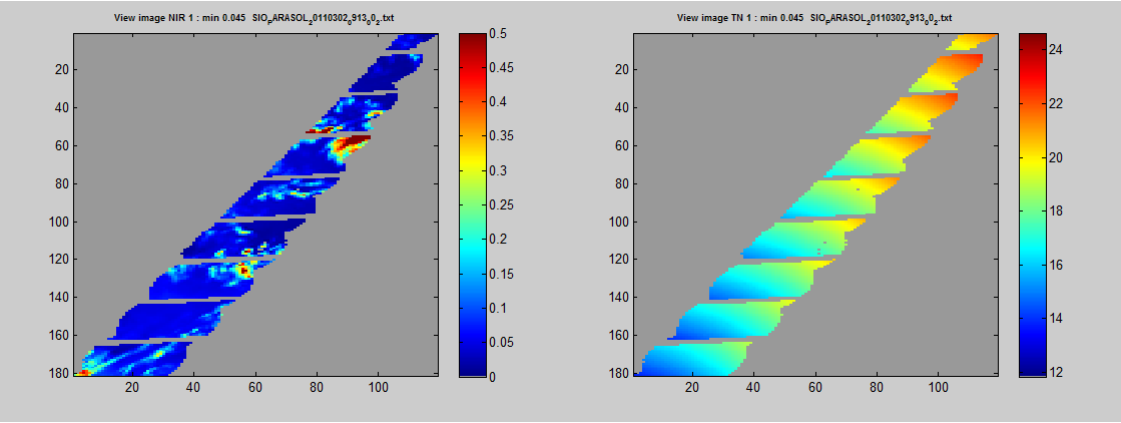

Figure 42: TOA reflectance inside Sunglint area (Left). Wave angle inside the sunglint area for PARASOL direction 1

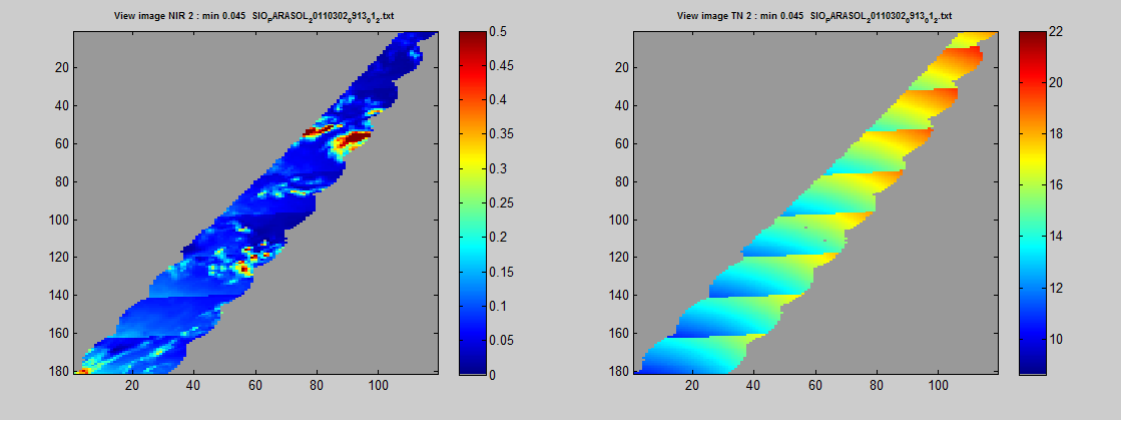

Figure 43: TOA reflectance inside Sunglint area (Left). Wave angle inside the sunglint area for PARASOL direction 2

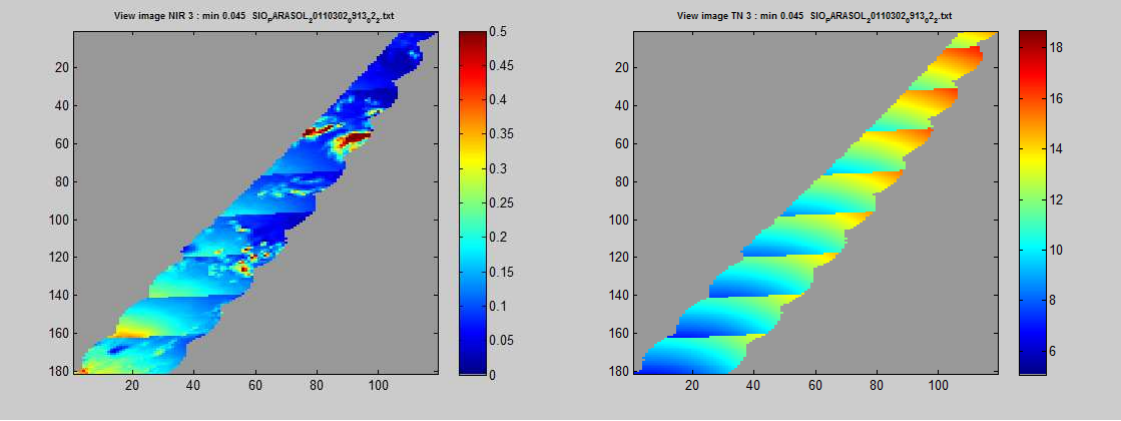

This document is the property of Magellium. It cannot be reproduced, nor communicated without written permission.

Figure 44: TOA reflectance inside Sunglint area (Left). Wave angle inside the sunglint area for PARASOL direction3

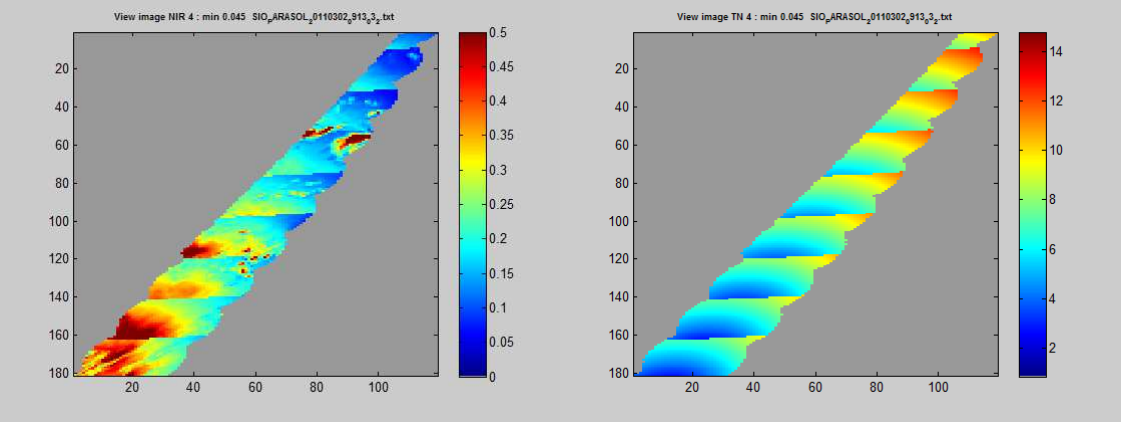

Figure 45: TOA reflectance inside Sunglint area (Left). Wave angle inside the sunglint area for PARASOL direction 4

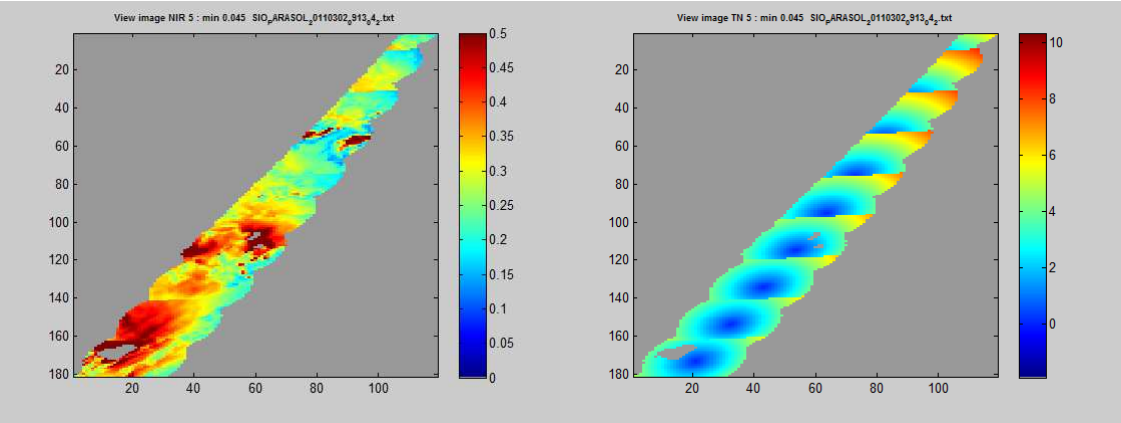

Figure 46: TOA reflectance inside Sunglint area (Left). Wave angle inside the sunglint area for PARASOL direction 5

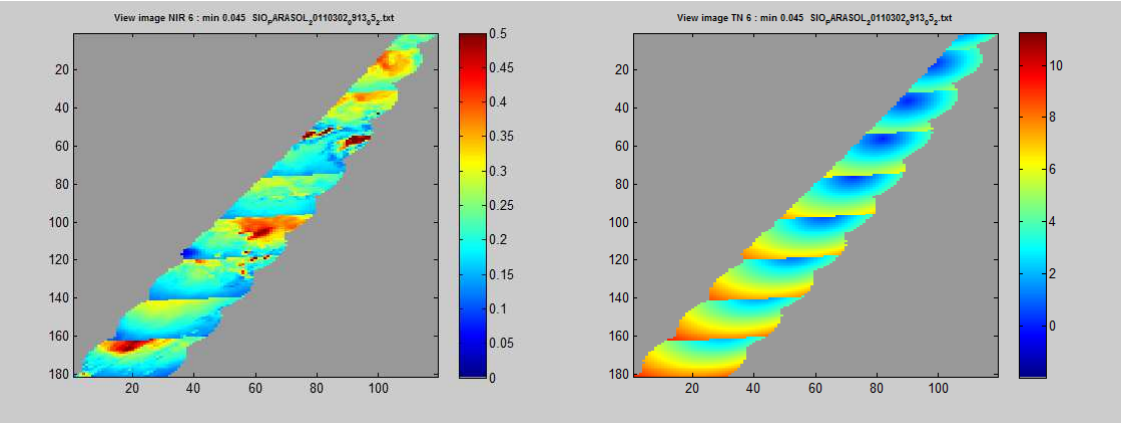

Figure 47: TOA reflectance inside Sunglint area (Left). Wave angle inside the sunglint area for PARASOL direction 6

This document is the property of Magellium. It cannot be reproduced, nor communicated without written permission.

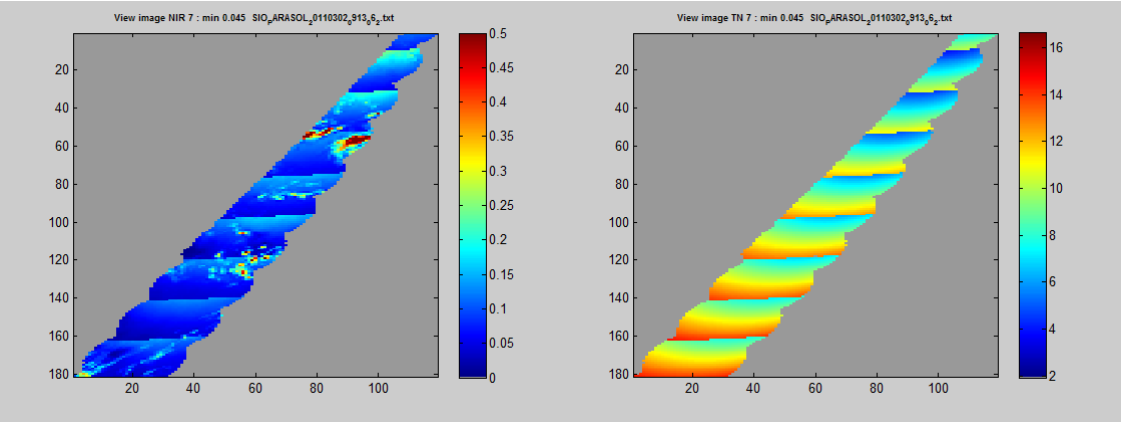

Figure 48: TOA reflectance inside Sunglint area (Left). Wave angle inside the sunglint area for PARASOL direction 7

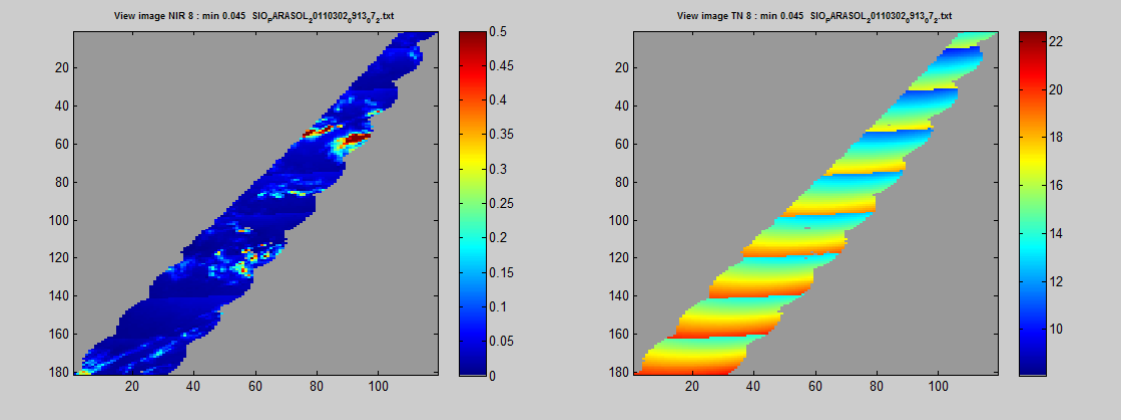

Figure 49: TOA reflectance inside Sunglint area (Left). Wave angle inside the sunglint area for PARASOL direction 8

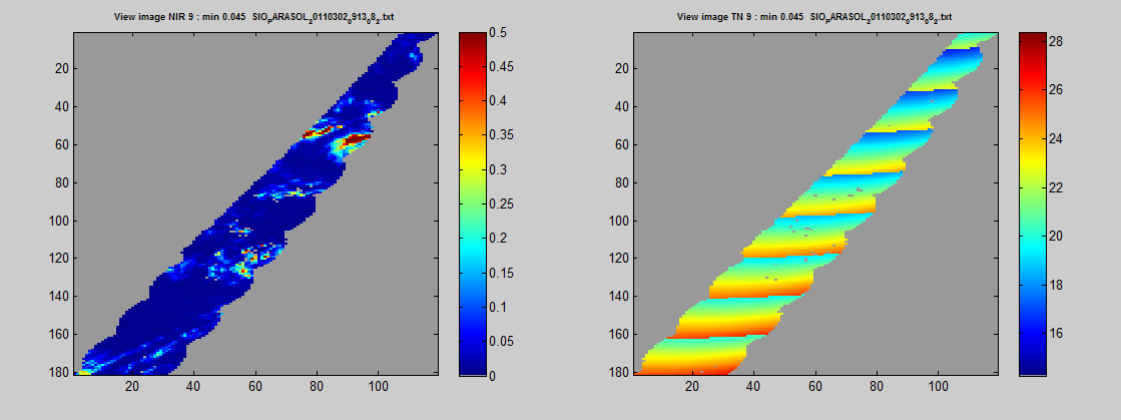

Figure 50: TOA reflectance inside Sunglint area (Left). Wave angle inside the sunglint area for PARASOL direction 9

This document is the property of Magellium. It cannot be reproduced, nor communicated without written permission.

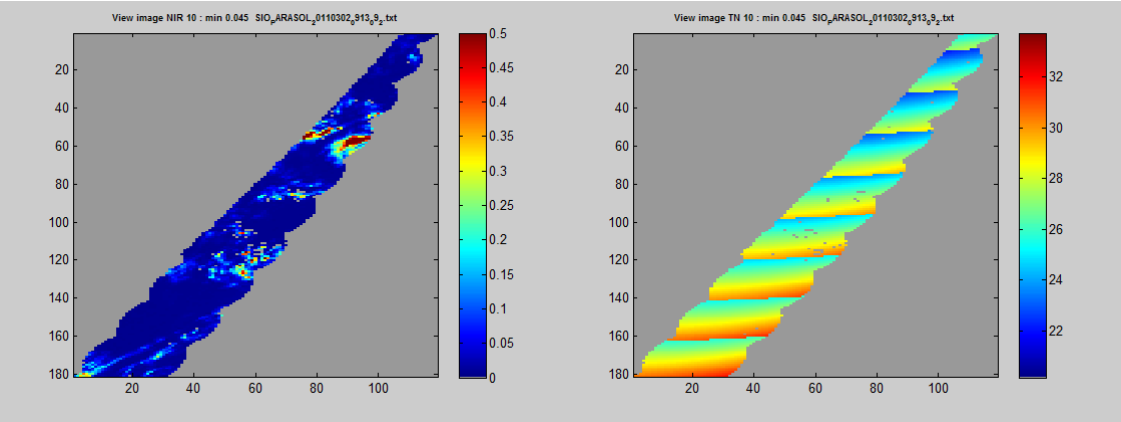

Figure 51: TOA reflectance inside Sunglint area (Left). Wave angle inside the sunglint area for PARASOL direction 10

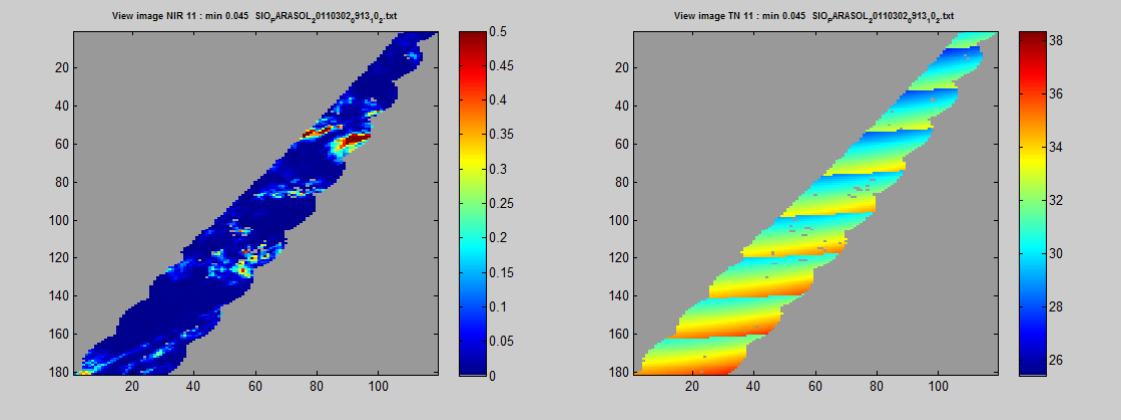

Figure 52: TOA reflectance inside Sunglint area (Left). Wave angle inside the sunglint area for PARASOL direction 11

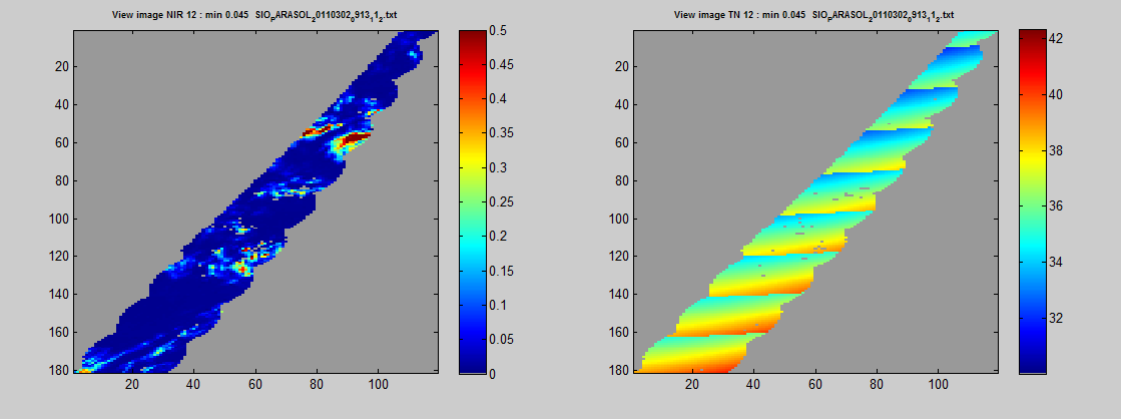

Figure 53: TOA reflectance inside Sunglint area (Left). Wave angle inside the sunglint area for PARASOL direction 12

This document is the property of Magellium. It cannot be reproduced, nor communicated without written permission.

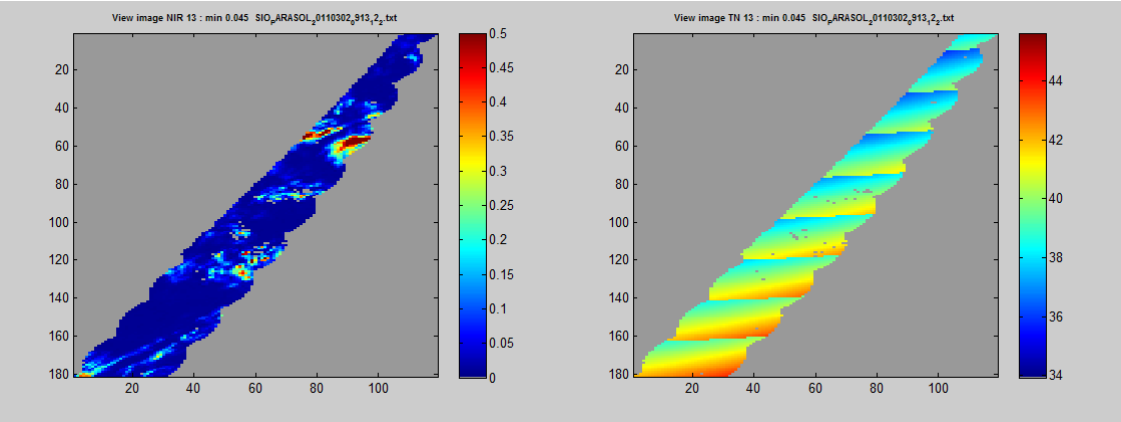

Figure 54: TOA reflectance inside Sunglint area (Left). Wave angle inside the sunglint area for PARASOL direction 13

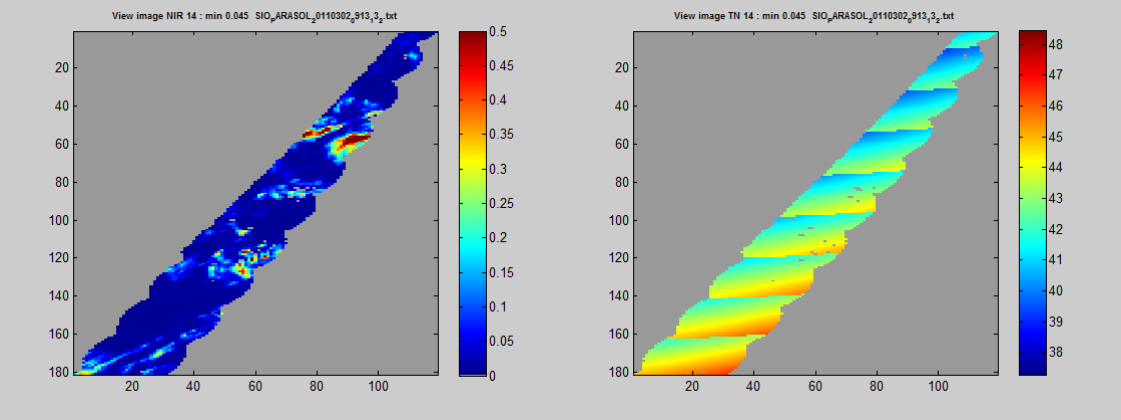

Figure 55: TOA reflectance inside Sunglint area (Left). Wave angle inside the sunglint area for PARASOL direction 14

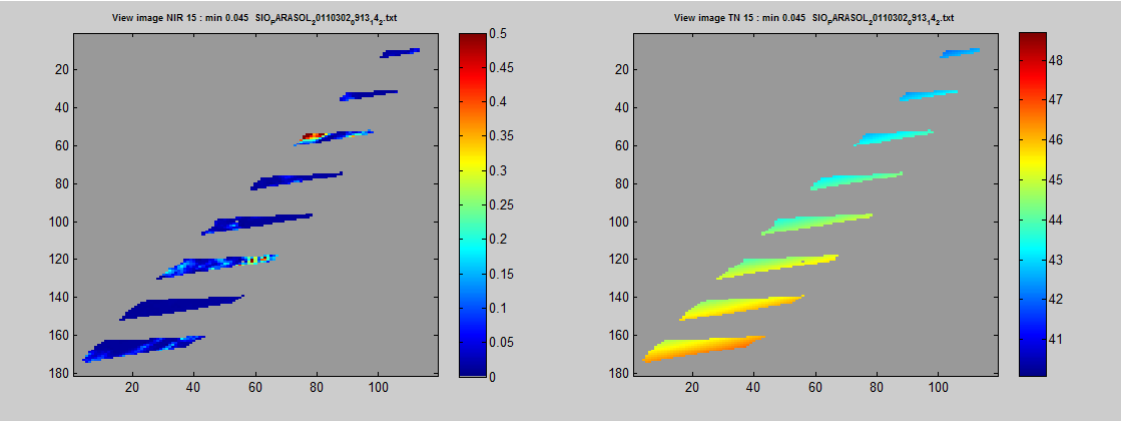

Figure 56: TOA reflectance inside Sunglint area (Left). Wave angle inside the sunglint area for PARASOL direction 15

A selection is performed to find for the selected pixels, the one which has the minimum wave angle and the maximum TOA reflectance in the NIR. Based on this test, we have selected the data that are used in the method. For this acquisition, we note that data acquired in directions 5 and 6 match the criteria.

This document is the property of Magellium. It cannot be reproduced, nor communicated without written permission.

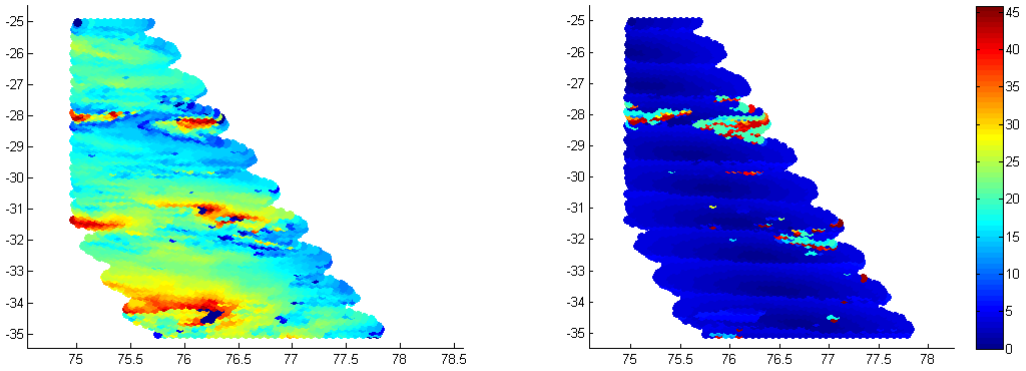

Figure 57: Maximum TOA reflectance inside Sunglint area (Left). Minimum wave angle computed from the 16 directions

Read auxiliary data

Wind speed, Water vapor content, and Ozone content are extracted from ERA datasets in the sunglint area

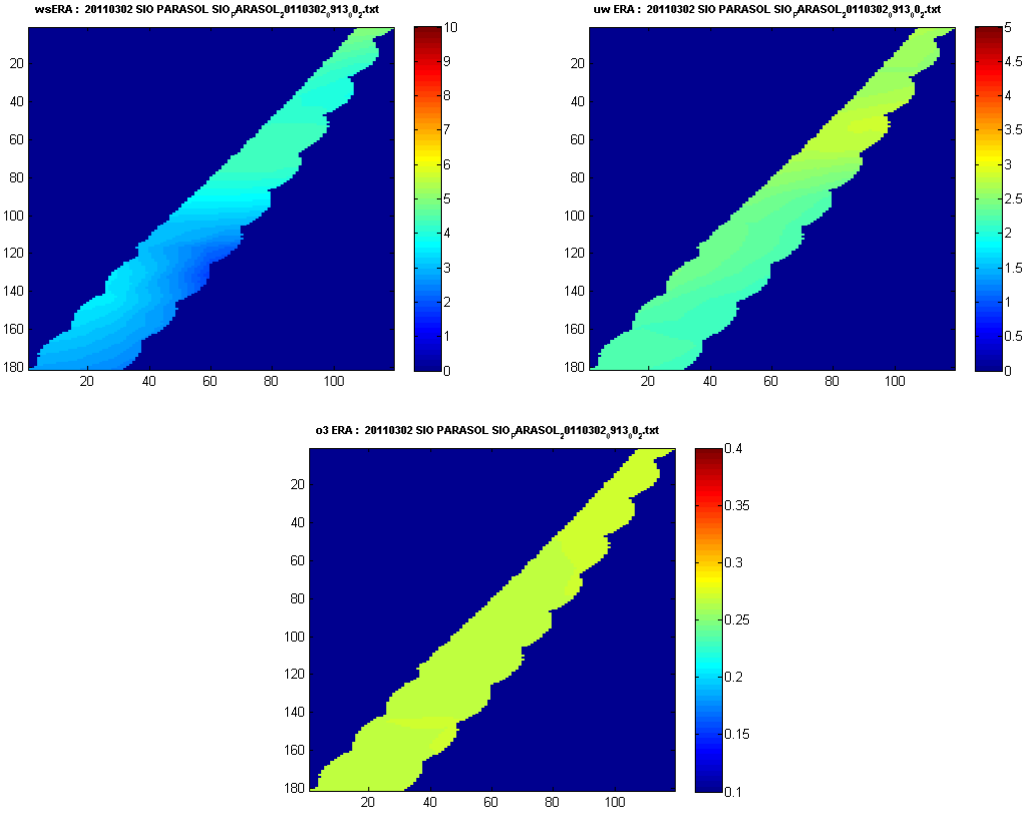

Figure 58: Windspeed, Water vapour content and ozone content

The sunglint area is a large area. The variability of the data for this date is low. Wind speed varies between 3 and 5 m/s. A mean level of ozone content around 0.27 cm.atm is observed and a water vapor is around 2.5 -3 g/cm^2.

This document is the property of Magellium. It cannot be reproduced, nor communicated without written permission.

Check Pixels selection test

After this step, the implementation of the method is exactly the same than the one used for MODIS and MERIS.

- Select valid pixels
- Select clear pixels
- Select NIR TOA pixels such as ρNIR > 0.15

A mask of valid pixel is applied is computed from the acquisition. These data are flagged inside the products, and the information is conserved in the data extracted from the ingestion module.

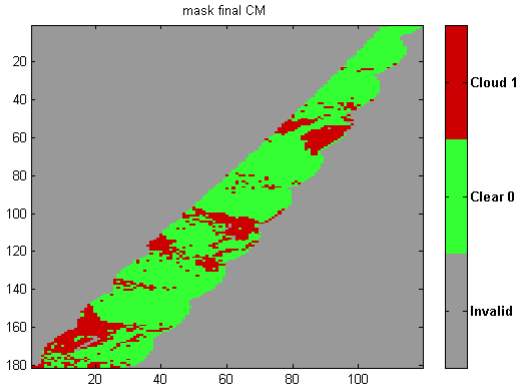

Figure 59: Cloud mask

Correct TOA reflectances from gaseous absorption

The comparison of TOA measurements to the simulated TOA reflectances is performed on TOA reflectance normalized to gaseous absorption.

The SMAC method allows to estimate the gaseous transmission for the atmospheric content read from ERA data at the date of acquisition. These coefficients are provided for each spectral bands used in the method.

Estimate wind speed in the reference band

The wind speed is derived based on a LUT of TOA reflectances generated with 6SV, for various wind speed. The wind speed value is selected such as the TOA reflectance measured agrees best with the modelled one.

This step is controlled using a scatterplot of TOA reflectance measured versus estimated. Any point diverging from the 1:1 line indicates a problem in the wind speed retrieval.

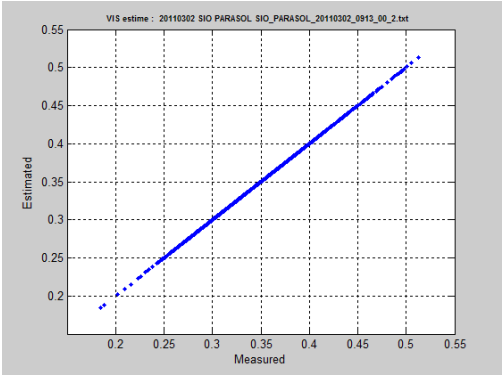

Figure 60: Control of the wind speed retrieval

This document is the property of Magellium. It cannot be reproduced, nor communicated without written permission.

The wind speed estimated using the LUT is analysed and only pixels for which wind speed is lower than 5 m/s are kept.

For this acquisition, the histogram of the retrieved wind speed is represented hereafter.

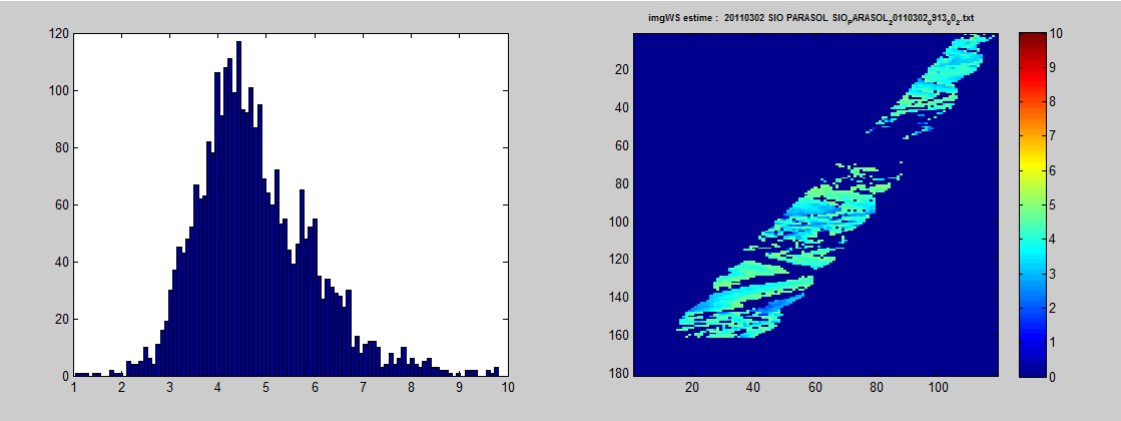

Figure 61: Estimated wind speed

Estimate the TOA reflectance in the bands for which radiometry is monitored using estimated wind speed

Once the wind speed estimated, it is used to simulate the TOA reflectances in the other channels.

The ratio of measured to estimated reflectance is computed for all the pixels selected in the area. The scatterplot is shown hereafter for the two bands, BLUE, and NIR.

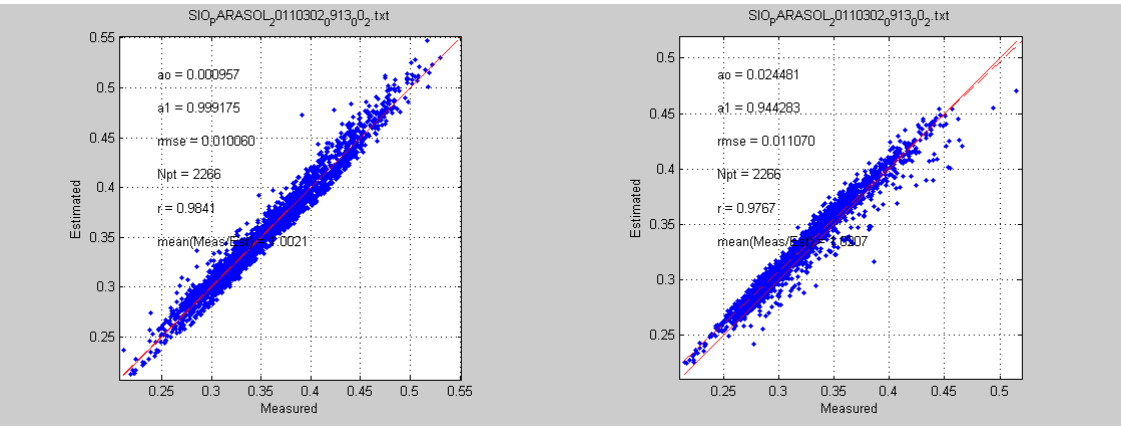

Figure 62: Scatterplot of simulated TOA reflectances versus measured TOA reflectances

At this step, an analysis is also performed to check that no correlation is observed between the reflectance ratio and the estimated wind speed.

This document is the property of Magellium. It cannot be reproduced, nor communicated without written permission.

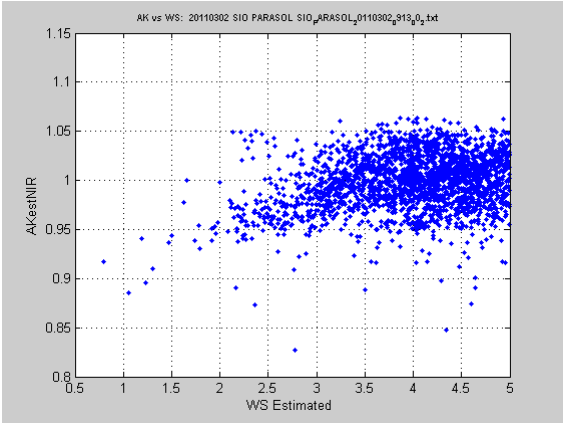

Figure 63: Measured to Simulated TOA reflectance ratio in the NIR versus estimated wind speed

Estimate the measured to simulated TOA reflectance ratio in the BLUE and NIR band

The map of ratio of measured to simulated TOA reflectance in the NIR channel is represented here after:

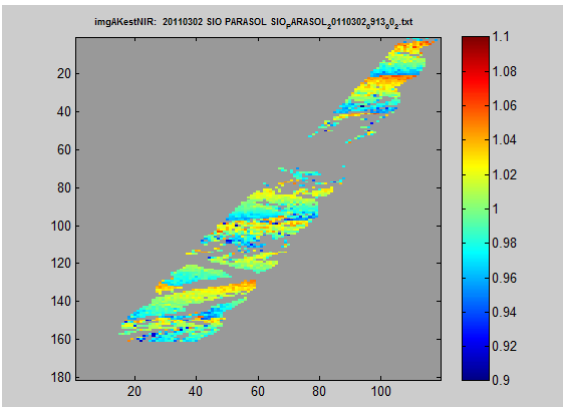

Figure 64: Map of Ak in the NIR band

The histograms of the ratio in the two bands are the following:

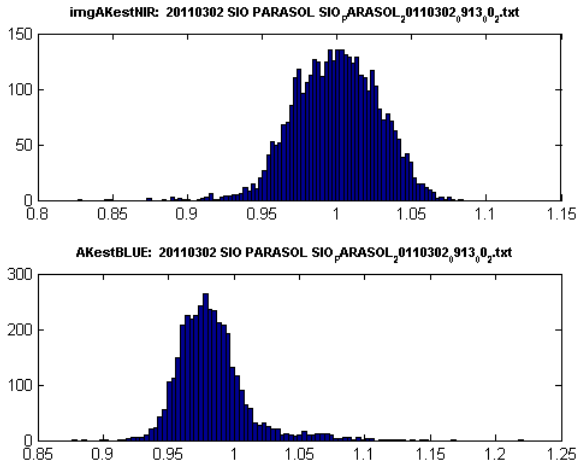

Figure 65: Reflectance ratio histograms (Top, NIR channel; Bottom, BLUE channel)

This document is the property of Magellium. It cannot be reproduced, nor communicated without written permission.

4.6.1.2 Multiyear results

The change in sensor radiometry is estimated by computing the mean of the measured to simulated TOA reflectances ratio for all available acquisitions (Eq. 19).

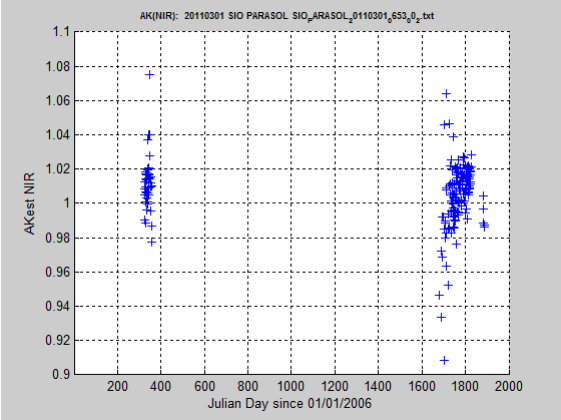

Figure 66: Temporal acquisition of mean ratio between 2006 and 2011 – NIR band

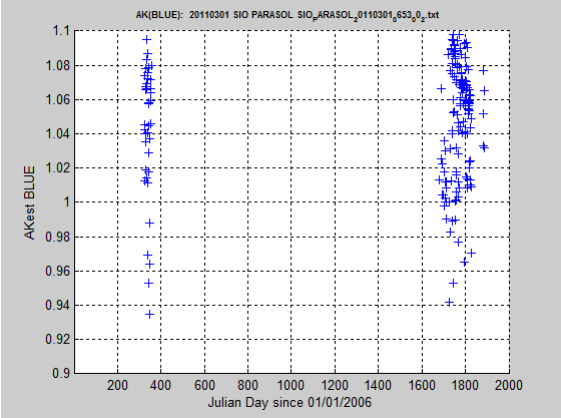

Figure 67: Temporal acquisition of mean ratio between 2006 and 2011 – BLUE band

4.7 Analysis of AASTR

4.7.1 Over SIO

No sunglint spot is identified using the pixel selection method. It has been extended to $\theta n < 7$, but it is not sufficient.

4.8 Analysis of ASTR-2

4.8.1 Over SIO

Not processed

This document is the property of Magellium. It cannot be reproduced, nor communicated without written permission.

5 Sensitivity study

5.1 Introduction

A sensitivity study is performed to assess the impact of a noise in the input data. A pixel on MERIS data has been chosen in acquisition of 23/11/2008 for which sunglint method has been applied.

The study is performed by using the radiative transfer 6SV.

5.2 Initial conditions

The values used in the method are the following:

Table 13: Input data

Variable	Reference
date	23/11/2008
θs	24.5123 deg
θv	22.9556 deg
dϕ	170.6216 deg
Aerosol model	Shettle and Fenn, Maritime 98
AOT 550nm	0.08
Water vapour content	1.44 g/cm2
Ozone content	0.3 cm.atm
Chlorophyll concentration	0.05 g/cm-3

The values of the TOA reflectance in all bands are the following.

Spectral band	B1	B2	B3	B4	B5
$\rho_{toa}(\lambda)$	0.267716	0.253647	0.2348	0.220003	0.206293
Spectral band	B6	B7	B8	B9	B10
$\rho_{toa}(\lambda)$	0.195759	0.209041	0.211976	0.202222	0.213979
Spectral band	B11	B12	B13	B14	B15
$\rho_{toa}(\lambda)$	0.076212	0.21422	0.210903	0.210889	0.138359

This document is the property of Magellium. It cannot be reproduced, nor communicated without written permission.

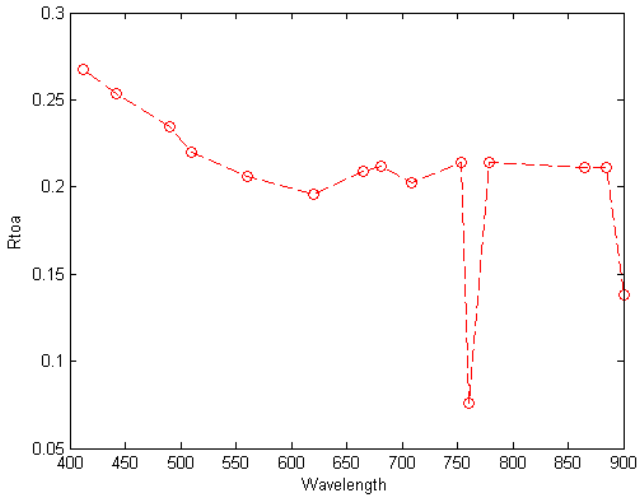

Figure 68: MERIS spectrum for the sensitivity study

For the reference, the Ak estimated in the NIR and BLUE band is:

Spectral band	Windspeed	AK (BLUE)	AK (NIR)
REF	4.1	1.06	0.98

5.3 Sensitivity to aerosol optical thickness

AOT	Estimated windspeed	AK (BLUE)	AK (NIR)
AOT=0.05	4.3	1.06051819	0.99760937
AOT=0.1	3.97	1.07071263	0.984746682

5.4 Sensitivity to water vapour content

UW	Estimated windspeed	AK (BLUE)	AK (NIR)
UW=2	4.1	1.070712635	0.9895212
UW=3	4.1	1.07071263	0.99012564

This document is the property of Magellium. It cannot be reproduced, nor communicated without written permission.

5.5 Sensitivity to ozone content

O3	Estimated windspeed	AK (BLUE)	AK (NIR)
0.27	4.1	1.06719657	0.98986494
0.29	4.1	1.06631062	0.98952126

5.6 Sensitivity to aerosol model

Model	Estimated windspeed	AK (BLUE)	AK (NIR)
Maritime	4.15	1.04719748	1.01929923
Maritime 2	4.15	1.05549437	1.01411372

5.7 Conclusion

The parameter which has the main impact is the model of aerosol. The reference level in the NIR is 0.98. It becomes 1.02 if the maritime model of 6S is used (characterised by the proportion of the following basic component, 0.95 water soluble and 0.05 oceanic component), and 1.015 if a maritime model with higher water soluble component is used (characterised by the proportion of the following basic component, 0.99 water soluble and 0.01 oceanic component).

Water vapour content accuracy has an impact in NIR band where the gas absorbs, whereas the level of aerosol optical thickness seems to have a very small impact.

However, to confirm the impact of the aerosol optical thickness and the aerosol type, Aerosol MODIS atmosphere dataset have been downloaded to assess the temporal variability of these variables. The data source is MODIS Atmosphere dataset, Monthly synthesis, for which the mean, the minimum and maximum observed values are available, and also the standard deviation.

The AOT at 550 nm and the angstrom coefficient are represented for the SIO oceanic site in the two next figures. As it can be observed, the variability is not low, even a mean value of AOT is around 0.08 for the 10 years of monthly products is seen. Associated to these variations are observed the variations of the angstrom coefficient, which varies between 0.2 and 1.2, with large variations of the mean values from one month to another one.

This document is the property of Magellium. It cannot be reproduced, nor communicated without written permission.

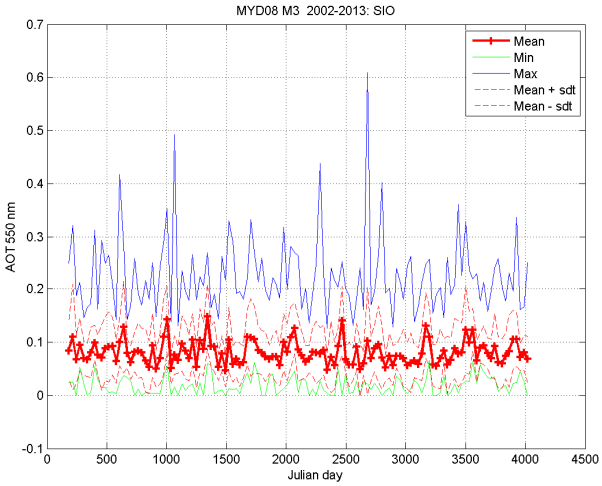

Figure 69: Aerosol optical thickness temporal variability since 06/2002 (Dataset MYD08_M3) over SIO

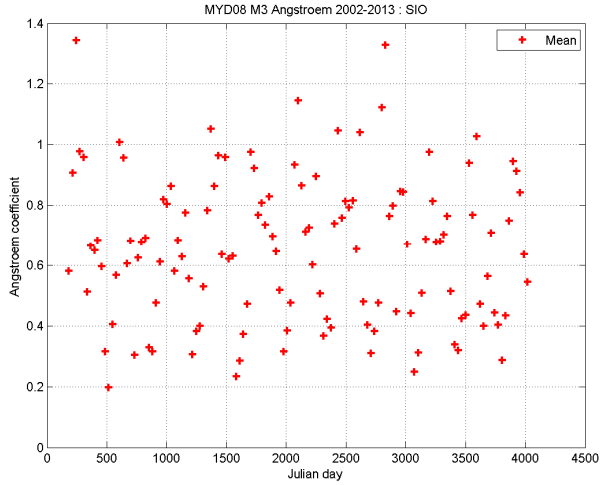

Figure 70: Angstrom exponent temporal variability since 06/2002 (Dataset MYD08_M3) over SIO

These observations indicate that the aerosol model is probably not the same over a year, neither the AOT. The use of this information could be a way to improve the results, either by adding new LUTS corresponding to another aerosol model, or by discarding data with a too high AOT.

For illustrating the impact of a change of the aerosol model, the spectral variability of the AOT for a collection of model is shown in the next figure.

This document is the property of Magellium. It cannot be reproduced, nor communicated without written permission.

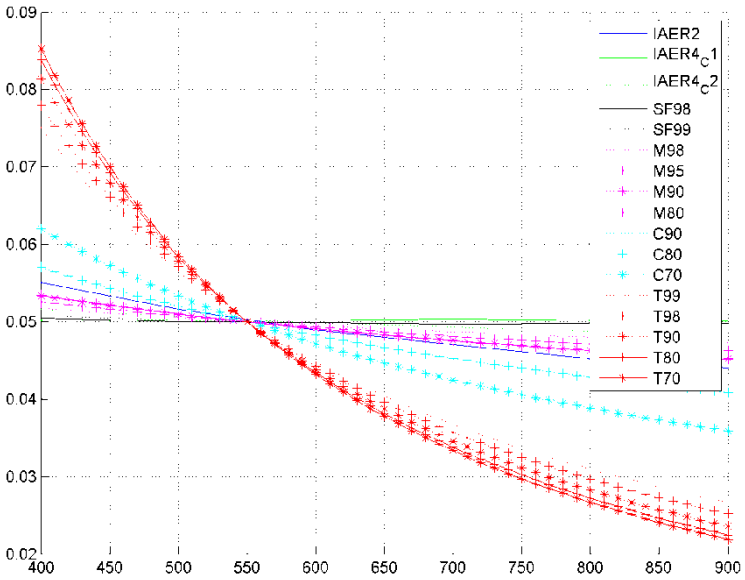

Figure 71: Spectral AOT variability for 17 models. AOT(550 nm)=0.05. M, C and T account for Maritime, Coastal and Tropospheric aerosols respectively. The number is the relative humidity according to the Shettle and Fenn classification.

This document is the property of Magellium. It cannot be reproduced, nor communicated without written permission.

6 Error analysis

Several authors (Hagolle et al, 2004; Jolivet et al. 2009) for instance have performed detailed error analysis for the sensor calibration using the sun glint method. The following list recaps the main post of uncertainties.

The uncertainties in the calibration include:

- Uncertainties in the radiative computation: If the solar zenith angle is smaller than 75°, the accuracy of the radiative transfer calculation based on plane parallel approximation is better than 10^{-3} in reflectance units (Vermote and Tanré, 1992).
- Calibration errors: Error on the reference band (Red band) involves error on the retrieved wind speed, therefore in the other spectral bands. Error in band calibration is assumed to be 3%.
- Geophysical uncertainties:
  - Gaseous absorption:
    - ozone amount : 5%
    - water vapour amount: 20%
  - Chlorophyll content. Water leaving radiance in spectral bands higher than 0.670 µm are not affected by errors on chlorophyll content. Only spectral nads lower than 0.67 µm are.
  - Rayleigh optical thickness: 1.5 % resulting from an error of 15 hPa on pressure.
  - aerosol type: low, 1.5%
  - Sea refraction index: this parameter controls the sea surface reflectivity:0.1% under 1100 nm, 0.3% above.
  - Foam is discarded using only pixels where the wind speed is lower than 5m/s.

- End of the document -

This document is the property of Magellium. It cannot be reproduced, nor communicated without written permission.